Mapping Protoplanetary Disk Vertical Structure with CO Isotopologue Line Emission

Charles J. Law[1][iD], Richard Teague[1,2][iD], Karin I. Öberg[1][iD], Evan A. Rich[3][iD], Sean M. Andrews[1][iD], Jaehan Bae[4][iD],
Myriam Benisty[5][iD], Stefano Facchini[6][iD], Kevin Flaherty[7][iD], Andrea Isella[8][iD], Sheng Jin[9][iD], Jun Hashimoto[10,11,12][iD],
Jane Huang[3,21][iD], Ryan A. Loomis[13][iD], Feng Long[1][iD], Carlos E. Muñoz-Romero[1][iD], Teresa Paneque-Carreño[14][iD],
Laura M. Pérez[15,16][iD], Chunhua Qi[1][iD], Kamber R. Schwarz[17][iD], Jochen Stadler[5,17][iD], Takashi Tsukagoshi[18,19][iD],
David J. Wilner[1][iD], and Gerrit van der Plas[20][iD]

[1] Center for Astrophysics | Harvard & Smithsonian, 60 Garden Street, Cambridge, MA 02138, USA
[2] Department of Earth, Atmospheric, and Planetary Sciences, Massachusetts Institute of Technology, Cambridge, MA 02139, USA
[3] Department of Astronomy, University of Michigan, 323 West Hall, 1085 South University Avenue, Ann Arbor, MI 48109, USA
[4] Department of Astronomy, University of Florida, Gainesville, FL 32611, USA
[5] Univ. Grenoble Alpes, CNRS, IPAG, F-38000 Grenoble, France
[6] European Southern Observatory, Karl-Schwarzschild-Str. 2, D-85748 Garching, Germany
[7] Department of Astronomy and Department of Physics, Williams College, Williamstown, MA 01267, USA
[8] Department of Physics and Astronomy, Rice University, 6100 Main Street, MS-108, Houston, TX 77005, USA
[9] CAS Key Laboratory of Planetary Sciences, Purple Mountain Observatory, Chinese Academy of Sciences, Nanjing 210008, People's Republic of China
[10] Astrobiology Center, National Institutes of Natural Sciences, 2-21-1 Osawa, Mitaka, Tokyo 181-8588, Japan
[11] Subaru Telescope, National Astronomical Observatory of Japan, Mitaka, Tokyo 181-8588, Japan
[12] Department of Astronomy, School of Science, Graduate University for Advanced Studies (SOKENDAI), Mitaka, Tokyo 181-8588, Japan
[13] National Radio Astronomy Observatory, 520 Edgemont Road, Charlottesville, VA 22903, USA
[14] European Southern Observatory, Karl-Shwarzschild-Strasse 2, D-85748 Garching bei Munchen, Germany
[15] Departamento de Astronomía, Universidad de Chile, Camino El Observatorio 1515, Las Condes, Santiago, Chile
[16] Núcleo Milenio de Formación Planetaria (NPF), Chile
[17] Max-Planck-Institut für Astronomie, Königstuhl 17, D-69117 Heidelberg, Germany
[18] National Astronomical Observatory of Japan, 2-21-1 Osawa, Mitaka, Tokyo 181-8588, Japan
[19] Faculty of Engineering, Ashikaga University, Ohmae-cho 268-1, Ashikaga, Tochigi, 326-8558, Japan
[20] Univ. Grenoble Alpes, CNRS, IPAG (UMR 5274), F-38000 Grenoble, France

Abstract

High-spatial-resolution observations of CO isotopologue line emission in protoplanetary disks at mid-inclinations ($\approx 30°$–$75°$) allow us to characterize the gas structure in detail, including radial and vertical substructures, emission surface heights and their dependencies on source characteristics, and disk temperature profiles. By combining observations of a suite of CO isotopologues, we can map the two-dimensional (r, z) disk structure from the disk upper atmosphere, as traced by CO, to near the midplane, as probed by less abundant isotopologues. Here, we present high-angular-resolution ($\lesssim 0\farcs1$ to $\approx 0\farcs2$; ≈ 15–30 au) observations of CO, ^{13}CO, and $C^{18}O$ in either or both $J = 2$–1 and $J = 3$–2 lines in the transition disks around DM Tau, Sz 91, LkCa 15, and HD 34282. We derived line emission surfaces in CO for all disks and in ^{13}CO for the DM Tau and LkCa 15 disks. With these observations, we do not resolve the vertical structure of $C^{18}O$ in any disk, which is instead consistent with $C^{18}O$ emission originating from the midplane. Both the $J = 2$–1 and $J = 3$–2 lines show similar heights. Using the derived emission surfaces, we computed radial and vertical gas temperature distributions for each disk, including empirical temperature models for the DM Tau and LkCa 15 disks. After combining our sample with literature sources, we find that ^{13}CO line emitting heights are also tentatively linked with source characteristics, e.g., stellar host mass, gas temperature, disk size, and show steeper trends than seen in CO emission surfaces.

Unified Astronomy Thesaurus concepts: Protoplanetary disks (1300); Planet formation (1241); CO line emission (262); High angular resolution (2167)

Supporting material: data behind figures, figure set

1. Introduction

Molecular line emission in protoplanetary disks originates from elevated surface layers above the disk midplanes (e.g., Dartois et al. 2003; Piétu et al. 2007; Rosenfeld et al. 2013; de Gregorio-Monsalvo et al. 2013). The vertical distribution of this molecular material depends on gradients in the physical conditions, such as temperature, density, and radiation, across the disk. It is also influenced by a variety of disk processes, e.g., the strength of turbulent vertical mixing (Ilgner et al. 2004; Semenov & Wiebe 2011; Flaherty et al. 2020) or the presence of meridional flows driven by embedded planets (Morbidelli et al. 2014; Teague et al. 2019; Yu et al. 2021).

Detailed knowledge of where line emission emanates is especially critical in interpreting a variety of observations, including kinematic signals in CO emission (Perez et al. 2015; Pérez et al. 2018, 2020; Pinte et al. 2019; Disk Dynamics Collaboration et al. 2020; Izquierdo et al. 2021; Teague et al. 2021; Wölfer et al. 2021), rotation-map-based dynamical stellar and disk mass estimates (Casassus & Pérez 2019;

---

[21] NASA Hubble Fellowship Program Sagan Fellow.

Paneque-Carreño et al. 2021; Veronesi et al. 2021), and signatures of planet–disk interactions versus depletions in gas surface density (Dong et al. 2019; Rab et al. 2020; Alarcón et al. 2021; Bae et al. 2021; Bollati et al. 2021; Calcino et al. 2022). The vertical distribution of line emission also has implications for the chemistry of planet formation, as molecular abundances are often derived from line emission that originates from elevated disk layers and not the planet-forming disk midplanes. Only with a detailed understanding of line emission heights can we assess the degree to which these abundances, especially those of potentially prebiotic molecules (e.g., Ilee et al. 2021), are linked to the planet-forming disk regions.

Observations of highly inclined or edge-on disks have provided valuable information about the vertical distribution of gas, as the emission distribution can be directly traced (Dutrey et al. 2017; Podio et al. 2020; Teague et al. 2020; Flores et al. 2021; Ruíz-Rodríguez et al. 2021; Villenave et al. 2022). However, due to the high angular resolution of the Atacama Large Millimeter/submillimeter Array (ALMA), we are no longer limited to edge-on sources to study disk vertical structure. It is now possible to spatially resolve elevated emission above and below the midplane even in mid-inclination ($\approx 30°$–$75°$) disks, which allows for a direct measurement of the emission heights of bright molecular lines (e.g., Pinte et al. 2018; Law et al. 2021a; Paneque-Carreño et al. 2021; Rich et al. 2021; Leemker et al. 2022; Paneque-Carreño et al. 2022; Stapper et al. 2023). This not only expands the number of disks where vertical information can be inferred, but also allows us to readily map both the radial and vertical disk structure.

Line emission surfaces have been the easiest to derive for CO, which is reflected in the substantial number of sources for which such data now exist (Pinte et al. 2018; Keppler et al. 2019; Teague et al. 2019; Law et al. 2021a, 2022; Rich et al. 2021; Izquierdo et al. 2022). CO alone, however, does not provide access to the full disk vertical structure, since it is typically emitting from $z/r > 0.2$, and therefore traces the uppermost layers in the disk atmospheres. Observations of rarer CO isotopologues with varying optical depths provide access to deeper layers closer to the disk midplane. This, in turn, allows us to infer vertical disk structure from atmosphere to midplane, including the gas temperature, which provides a powerful empirical input for disk thermo-chemical models (e.g., Calahan et al. 2021; Schwarz et al. 2021; Zhang et al. 2021).

Here, we extract emission surfaces in a set of CO isotopologue lines from four disks with favorable orientations with respect to our line of sight that have been previously observed at sufficiently high spatial resolution and sensitivity. In Section 2, we describe the calibration and imaging of the ALMA archival data, and in Section 3 we briefly detail our surface extraction methods. We present the derived emission surfaces along with radial and vertical temperature profiles in Section 4, and explore the origins of the observed disk vertical structure in Section 5. We summarize our conclusions in Section 6.

2. Observations

2.1. Archival Data and Observational Details

We searched the ALMA archive for observations of protoplanetary disks with inclinations of $30°$–$75°$ that covered several CO isotopologues in one or more lines, namely CO, ^{13}CO, and $C^{18}O$, and $J = 2$–1 and $J = 3$–2. We restricted our search to those sources observed at sufficiently high angular resolutions ($\lesssim 0\rlap{.}''3$),

line sensitivities (a few kelvins), and velocity resolutions ($\lesssim 0.25$ km s^{-1}) necessary to derive emission surfaces. After excluding previously published sources (Law et al. 2021a, 2022; Paneque-Carreño et al. 2021, 2022, 2023; Rich et al. 2021), we identified four such sources—the disks around DM Tau, Sz 91, LkCa 15, and HD 34282.

All data were obtained from the ALMA archive, except for the $J = 3$–2 lines of CO, ^{13}CO, and $C^{18}O$ in the LkCa 15 disk (Jin et al. 2019) and for CO $J = 3$–2 in the HD 34282 disk (van der Plas et al. 2017), which were taken from previously published ALMA observations. To achieve the necessary data quality, we often combined multiple programs and executions. Each observational program is listed in Table 2 and described in detail in Appendix A.

2.2. Self-calibration and Imaging

Each archival project was initially calibrated by ALMA staff using the ALMA calibration pipeline and the required version of CASA (McMullin et al. 2007). Subsequent self-calibration was performed using CASA v5.4.0 for all sources, except for Sz 91, where we were unable to derive solutions that improved image quality.

Our self-calibration strategy closely followed that of the MAPS ALMA Large Program, which is described in detail by Öberg et al. (2021). We created pseudo-continuum visibilities by flagging line emission in each spectral window, which were then combined with continuum-only spectral windows, when available. We then averaged down these data into 125 MHz channels, imaged each execution block, and measured the phase centers with the `imfit` task in CASA. To account for any source proper motions or atmospheric/instrumental effects between observations, we aligned each execution block to a common phase center using the `fixvis` and `fixplanets` tasks to apply the necessary phase shifts and assign common labels to the phase centers, respectively.

We first self-calibrated the aligned, short-baseline data. When multiple short-baseline observations were available, all executions were initially concatenated together. Then, we concatenated the self-calibrated short-spacing data with the long-baseline data, and the combined visibilities were self-calibrated together. We considered phase solution intervals beginning at infinity and decreasing to 60 s, or stopping sooner if the signal-to-noise ratio (S/N) of the data did not improve. When it resulted in a S/N improvement, a single round of amplitude self-calibration was performed on the combined visibilities with an infinite solution interval. The self-calibration typically improved the continuum S/N by a factor of 2–3. We ultimately applied the resulting calibration solutions to the unflagged and spectrally nonaveraged visibilities, before subtracting the continuum with a first-order polynomial using the `uvcontsub` task.

We then switched to CASA v6.3.0 for all imaging. We used `tclean` to produce images of the $J = 2$–1 lines of CO, ^{13}CO, and $C^{18}O$ for each source with Briggs weighting and Keplerian masks generated with the `keplerian_mask` (Teague 2020) code. Each mask was based on the stellar+disk parameters listed in Table 1 and was visually inspected to ensure that it contained all emission present in the channel maps. If required, manual adjustments to mask parameters were made, e.g., maximum radius and beam convolution size. Briggs `robust` parameters were chosen manually to prioritize spatially resolved and well-defined line emission in the channel maps (see Appendix B). Channel spacings ranged from 0.08 to

Table 1
Stellar and Disk Characteristics

Source	Spectral Type	Distance[a] (pc)	Incl. (°)	PA (°)	M_*[b] $(M_\odot)$	L_* $(L_\odot)$	Age[c] (Myr)	v_{sys}[b] (km s^{-1})	Cloud Contam.
DM Tau	M1 [1]	143	$36.0^{+0.12}_{-0.09}$ [2]	154.5 ± 0.24 [3]	0.53 ± 0.02	0.24 [1]d	3–7 [1]	5.99 ± 0.04	…
Sz 91	M0 [4]	158	49.7 ± 0.2 [5]	17.0 ± 0.26 [3]	0.54 ± 0.07	0.26 ± 0.02 [5]	3–7 [5,6]	3.39 ± 0.04	Moderate
LkCa 15	K5 [7]	157	50.2 ± 0.03 [8]	61.9 ± 0.04 [8]	1.20 ± 0.07	$1.05^{+0.27}_{-0.21}$ [7]	1–5 [1,7]	6.28 ± 0.04	…
HD 34282	A0-A1 [10]	306	59.3 ± 0.4 [9]	117.1 ± 0.3 [9]	1.69 ± 0.07	14.5 ± 0.7 [10]	4–7 [11]	-2.35 ± 0.01	…

Notes.
[a] All distances are from Gaia Early Data Release 3 (Gaia Collaboration et al. 2021; Bailer-Jones et al. 2021).
[b] Dynamical stellar masses and systemic velocities (in the LSR frame) are derived in this work and represent the mean values computed from all available CO isotopologues (see Appendix D).
[c] Stellar ages are likely uncertain by at least a factor of 2.
[d] Pegues et al. (2020) do not provide uncertainties on the stellar luminosity of DM Tau.
References: (1) Pegues et al. (2020), (2) Flaherty et al. (2020), (3) Law et al. (2022), (4) Romero et al. (2012), (5) Maucó et al. (2020), (6) Tsukagoshi et al. (2019), (7) Donati et al. (2019), (8) Facchini et al. (2020), (9) van der Plas et al. (2017), (10) Guzmán-Díaz et al. (2021), (11) Vioque et al. (2018).

Table 2
CO Isotopologue Image Cube Properties

Source Transition	Beam ($'' \times ''$, deg)	JvM ϵ[a]	robust	uv-taper ($''$)	Chan. δv (km s^{-1})	rms[b] (mJy beam^{-1}, K)	ALMA Project Code(s)
DM Tau							
CO $J = 2$–1	$0.13 \times 0.12, -37.9$	0.37	0.5	0.075	0.08	1.0, 1.5	2013.1.00498.S, 2016.1.00724.S, 2017.1.01460.S
^{13}CO $J = 2$–1	$0.20 \times 0.18, -46.1$	0.48	0.5	0.150	0.08	1.5, 1.0	2016.1.00724.S, 2017.1.01460.S
C^{18}O $J = 2$–1	$0.20 \times 0.18, -44.0$	0.49	0.5	0.150	0.08	1.1, 0.8	2016.1.00724.S, 2017.1.01460.S
Sz 91							
CO $J = 2$–1	$0.23 \times 0.16, 17.5$	0.41	0.5	…	0.16	2.1, 1.3	2013.1.00663.S, 2013.1.01020.S, 2015.1.01301.S
^{13}CO $J = 2$–1	$0.24 \times 0.17, 21.9$	0.41	0.5	…	0.20	2.2, 1.4	2013.1.00663.S, 2013.1.01020.S, 2015.1.01301.S
C^{18}O $J = 2$–1	$0.41 \times 0.38, 30.0$	0.21	2.0	0.300	0.20	0.8, 0.1	2013.1.00663.S, 2013.1.01020.S, 2015.1.01301.S
LkCa 15							
CO $J = 2$–1	$0.37 \times 0.27, -9.2$	0.73	0.0	…	0.20	2.3, 0.4	2013.1.00226.S, 2018.1.01255.S
^{13}CO $J = 2$–1	$0.14 \times 0.10, -18.8$	0.38	0.0	0.070	0.25	0.7, 1.3	2018.1.00945.S
C^{18}O $J = 2$–1	$0.18 \times 0.14, 10.0$	0.14	2.0	…	0.25	0.2, 0.2	2018.1.00945.S
HD 34282							
CO $J = 2$–1	$0.11 \times 0.09, -69.7$	0.21	−2.0	…	0.08	0.4, 1.0	2015.1.00192.S, 2017.1.01578.S
^{13}CO $J = 2$–1	$0.12 \times 0.10, -69.9$	0.16	−2.0	…	0.20	0.2, 0.5	2015.1.00192.S, 2017.1.01578.S
C^{18}O $J = 2$–1	$0.12 \times 0.10 -70.2$	0.16	−2.0	…	0.20	0.2, 0.4	2015.1.00192.S, 2017.1.01578.S

Notes.
[a] The ratio of the CLEAN beam and dirty beam effective area used to scale image residuals to account for the effects of non-Gaussian beams. See Section 2.2 and Jorsater & van Moorsel (1995) and Czekala et al. (2021) for further details.
[b] rms values were calculated for the corresponding image cube channel (δv) and brightness temperatures were calculated assuming the Rayleigh–Jeans limit.

0.25 km s^{-1} depending on the source and line. For several images, we also applied Gaussian uv-tapers of 0″070–0″150 to improve sensitivity to larger-scale emission. All images were made using the multiscale deconvolver with pixel scales of [0, 5, 15, 25], except for the CO $J = 2$–1 image in LkCa 15, which used [0, 8, 16, 32, 64]. All images were CLEANed down to a 4σ level, where σ was the rms measured in a line-free channel of the dirty image. Table 2 summarizes all image properties, including the ALMA project codes from which each image was generated.

After generating the image cubes, we applied the "JvM" correction proposed in Jorsater & van Moorsel (1995) and described in more detail in Czekala et al. (2021). This correction scales the image residuals by a factor, ϵ, equal to the ratio of the effective areas of the CLEAN beam and dirty beam, to be in units consistent with the CLEAN model. Table 2 lists all ϵ values. While we used the JvM-corrected images here, we have also verified that line emission surfaces extracted from either the JvM- or non-JvM-corrected images yield consistent results.

We also imaged the non-continuum-subtracted line data and the continuum data by adopting the same imaging parameters as the line-only emission image cubes. The non-continuum-subtracted image cubes were required for the calculation of gas temperatures (Section 4.5) and provided an additional check that continuum subtraction did not influence the extracted emission surfaces, while the continuum images were used to define the disk centers. The line-only and line+continuum image cubes, as well as all zeroth moment maps, are publicly available.[22]

2.3. Source Details and Moment Maps

All four sources in our sample host transition disks and span a range in stellar properties, such as masses (0.53–1.69 $M_\odot$), spectral types (M0–A1) and bolometric luminosities (0.24–14.5 $L_\odot$), and disk characteristics, such as overall CO emission radial extents ($\approx$400–1000 au). Table 1 shows a summary of source characteristics.

---

[22] doi:10.5281/zenodo.7430257.
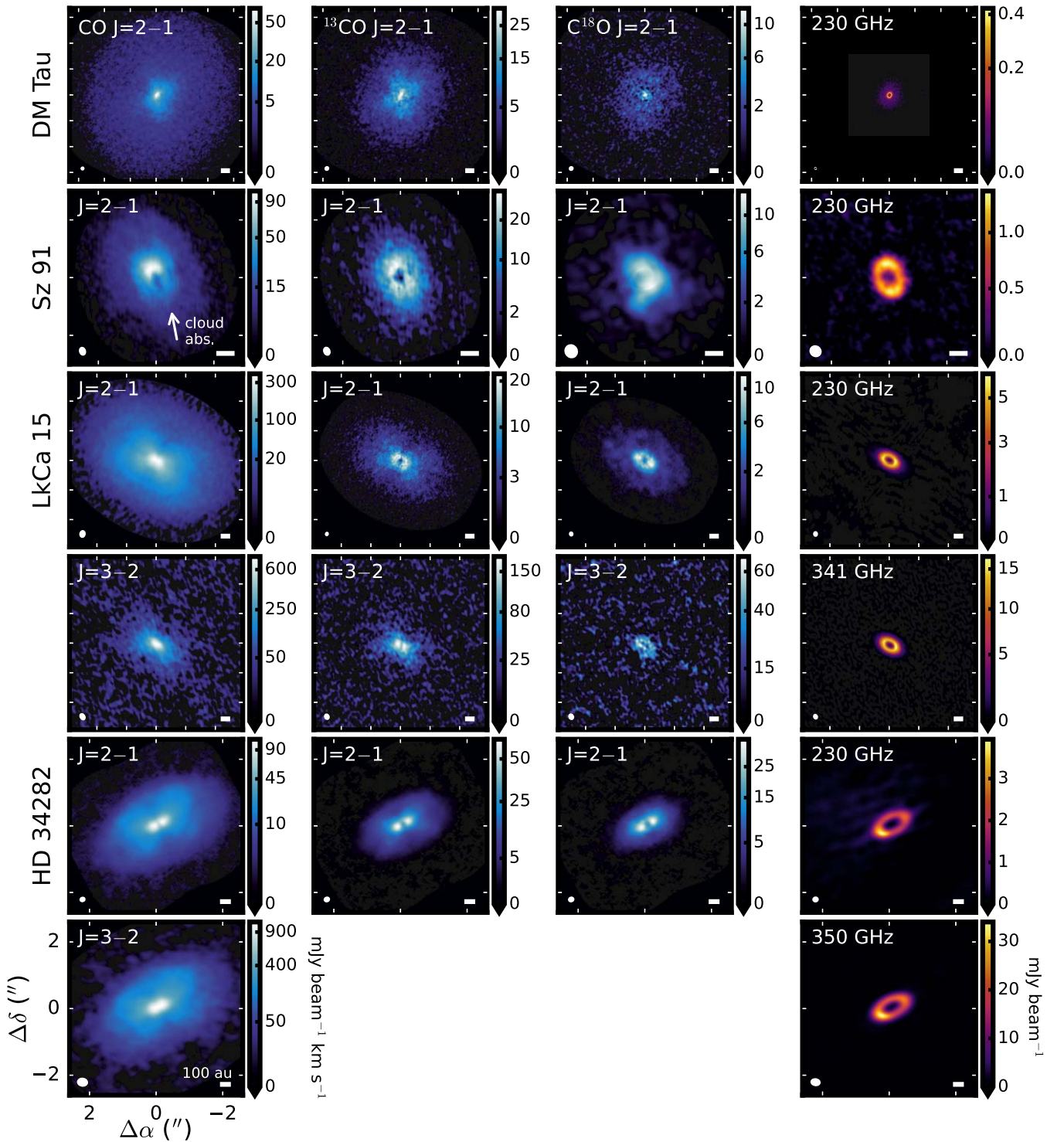
Figure 1. CO, ^{13}CO, and C^{18}O zeroth moment maps and continuum images (from left to right) for all sources in the sample, ordered from top to bottom by increasing stellar mass. Line emission is $J = 2-1$ and continuum is at 230 GHz, except for the fourth and sixth rows, which show the $J = 3-2$ line and 341 GHz or 350 GHz continuum emission in the LkCa 15 and HD 34282 disks, respectively. Panels for each disk have the same field of view, with each tick mark representing $2''$. Color stretches were individually optimized and applied to each panel to increase the visibility of outer disk structure. The asymmetry present in CO $J = 2-1$ in the Sz 91 disk is due to cloud contamination (e.g., Canovas et al. 2015; Tsukagoshi et al. 2019) and is labeled in the corresponding panel. The synthesized beam and a scale bar indicating 100 au is shown in the lower left and lower right corners, respectively, of each panel. Details about each of the observations are found in Table 1.

Figure 1 shows an overview of the disk sample in CO isotopologue velocity-integrated intensity, or "zeroth moment," maps, and in millimeter continuum emission. All continuum images were generated from the corresponding programs from which the line images were produced. We generated zeroth moment maps of line emission from the image cubes using `bettermoments` (Teague & Foreman-Mackey 2018) and closely followed the procedures outlined in Law et al. (2021b). We did not use a flux threshold for pixel inclusion, i.e., sigma clipping, to ensure accurate flux recovery and used the same Keplerian masks employed during CLEANing.

Table 3
Parameters for CO Isotopologue Emission Surface Fits

Source	Line	Exponentially Tapered Power Law				
		$r_{\text{fit, max}}$ ($''$)	z_0 ($''$)	ϕ	r_{taper} ($''$)	ψ
DM Tau	CO $J = 2-1$	2.70	$0.63^{+0.01}_{-0.01}$	$1.81^{+0.02}_{-0.02}$	$[2.00]^{\text{a}}$	$1.51^{+0.03}_{-0.03}$
	^{13}CO $J = 2-1^{\text{b}}$	1.30	$0.22^{+0.00}_{-0.00}$	$1.14^{+0.02}_{-0.02}$	...	...
Sz 91	CO $J = 2-1^{\text{b}}$	2.50	$0.16^{+0.01}_{-0.01}$	$0.72^{+0.05}_{-0.05}$	...	...
LkCa 15	CO $J = 2-1$	4.75	$0.25^{+0.00}_{-0.00}$	$1.42^{+0.06}_{-0.05}$	$3.65^{+0.07}_{-0.08}$	$3.39^{+0.26}_{-0.25}$
	^{13}CO $J = 2-1$	2.25	$0.16^{+0.07}_{-0.02}$	$1.27^{+0.44}_{-0.29}$	$1.93^{+0.19}_{-0.42}$	$3.22^{+1.59}_{-1.26}$
	CO $J = 3-2$	5.00	$0.20^{+0.02}_{-0.01}$	$2.27^{+0.22}_{-0.17}$	$2.64^{+0.29}_{-0.36}$	$2.02^{+0.29}_{-0.27}$
	^{13}CO $J = 3-2$	2.75	$0.17^{+0.02}_{-0.01}$	$1.14^{+0.24}_{-0.13}$	$2.60^{+0.14}_{-0.27}$	$3.76^{+0.90}_{-1.46}$
HD 34282	CO $J = 2-1$	1.50	$0.83^{+0.02}_{-0.05}$	$1.37^{+0.04}_{-0.04}$	$1.03^{+0.05}_{-0.02}$	$1.41^{+0.07}_{-0.05}$
	CO $J = 3-2$	2.00	$0.38^{+0.02}_{-0.02}$	$0.80^{+0.10}_{-0.08}$	$1.65^{+0.03}_{-0.04}$	$4.36^{+0.66}_{-0.59}$

Notes.
[a] Due to parameter degeneracies encountered when fitting the extended, elevated emission, we fixed r_{taper}.
[b] Single power-law profiles were used.

The Sz 91 disk exhibits moderate cloud contamination in CO $J = 2-1$ between $v_{\text{LSR}} \approx 4$ and 7 km s^{-1}, in which the ambient cloud significantly absorbs disk line emission with overlapping velocities. This is identified through visual inspection of channel maps (Appendix B) and manifests as a north–south spatial brightness asymmetry in images of the CO line emission (see Figure 1). Cloud obscuration was previously identified in this disk in a similar velocity range in the CO $J = 3-2$ line (Canovas et al. 2015; Tsukagoshi et al. 2019).

3. Methods

3.1. Surface Extraction

We derived vertical emission heights on a per-pixel basis directly from the line emission image cubes using the `disksurf` (Teague et al. 2021) Python code, based on the methodology presented in Pinte et al. (2018). We closely followed the methods outlined in Law et al. (2021a), which we briefly summarize below.

Before extraction, we first masked the image cubes with the same Keplerian masks used during CLEANing and manually excluded all channels where the front and back disk sides could not be clearly distinguished. We adopted an inclination and position angle (PA) for each disk (Table 1), which yields a deprojected radius r, emission height z, surface brightness I_ν, and channel velocity v for each pixel associated with the emitting surface.

We then filtered pixels based on priors of expected disk physical structure, i.e., removing those pixels with unphysically high z/r or large negative z values, as the emission must arise from at least the midplane. To avoid positively biasing our averages to nonzero z values, we did not remove those with small negative values, i.e., $z/r > -0.1$. For the HD 34282 disk, we instead only removed pixels with $z/r < 0.05$ to mitigate confusion due to the high inclination of this source and visually confirmed that the resulting surface was not artificially distorted by this cut. To avoid the misidentification of peaks due to noise, we also filtered pixels with low surface brightnesses, ranging from $1\times$ rms (Sz 91) to $6\times$ rms (HD 34282). The wide range in thresholds was a result of our heterogeneous sample with differing line sensitivities. Throughout this process, we prioritized obtaining the maximum number of robust emission

surface pixels and at each step visually confirmed the fidelity of derived surfaces.

After completing these filtering steps, we binned the surfaces in two ways: (i) into radial bins equal to half of the FWHM of the beam major axis; and (ii) by computing a moving average with a minimum window size of $1/2\times$ the beam major axis FWHM. While both methods are effective at reducing scatter in the extracted surfaces, the radially binned surfaces benefit from a uniform radial sampling, while the moving averages maintain a finer radial sampling that is sensitive to subtle vertical perturbations, e.g., from putative embedded planets. In some cases, we radially bin these surfaces further for visual clarity, but all quantitative analysis is performed with the original binning of each type of emission surface. All three types of line emission surfaces—individual measurements, radially binned, and moving averages—are made publicly available as data behind the figure.

3.2. Analytical Fitting

We fitted parametric models to all line emission surfaces to facilitate comparisons with other observations and incorporation into models. For the majority of sources and lines, we use the form of an exponentially tapered power law, which describes the flared inner surfaces as well as the plateau and turnover region at larger radii. We adopted the same functional form as in Law et al. (2021a):

$$z(r) = z_0 \times \left(\frac{r}{1''}\right)^\phi \times \exp\left(-\left[\frac{r}{r_{\text{taper}}}\right]^\psi\right). \quad (1)$$

However, in a few cases the derived surface was not well fitted by an exponentially tapered power-law profile, as no turnover of the emission surface was detectable (as discussed in detail in the following section). In those cases, we adopted a single power-law profile.

We used the Monte Carlo Markov Chain (MCMC) sampler implemented in `emcee` (Foreman-Mackey et al. 2013) to estimate the posterior probability distributions for z_0, ϕ, r_{taper}, and ψ. Each ensemble uses 64 walkers with 1000 burn-in steps and an additional 500 steps to sample the posterior distribution function. Table 3 shows the median values of the posterior distribution, with uncertainties given as the 16th and 84th percentiles. We stress that these represent the statistical
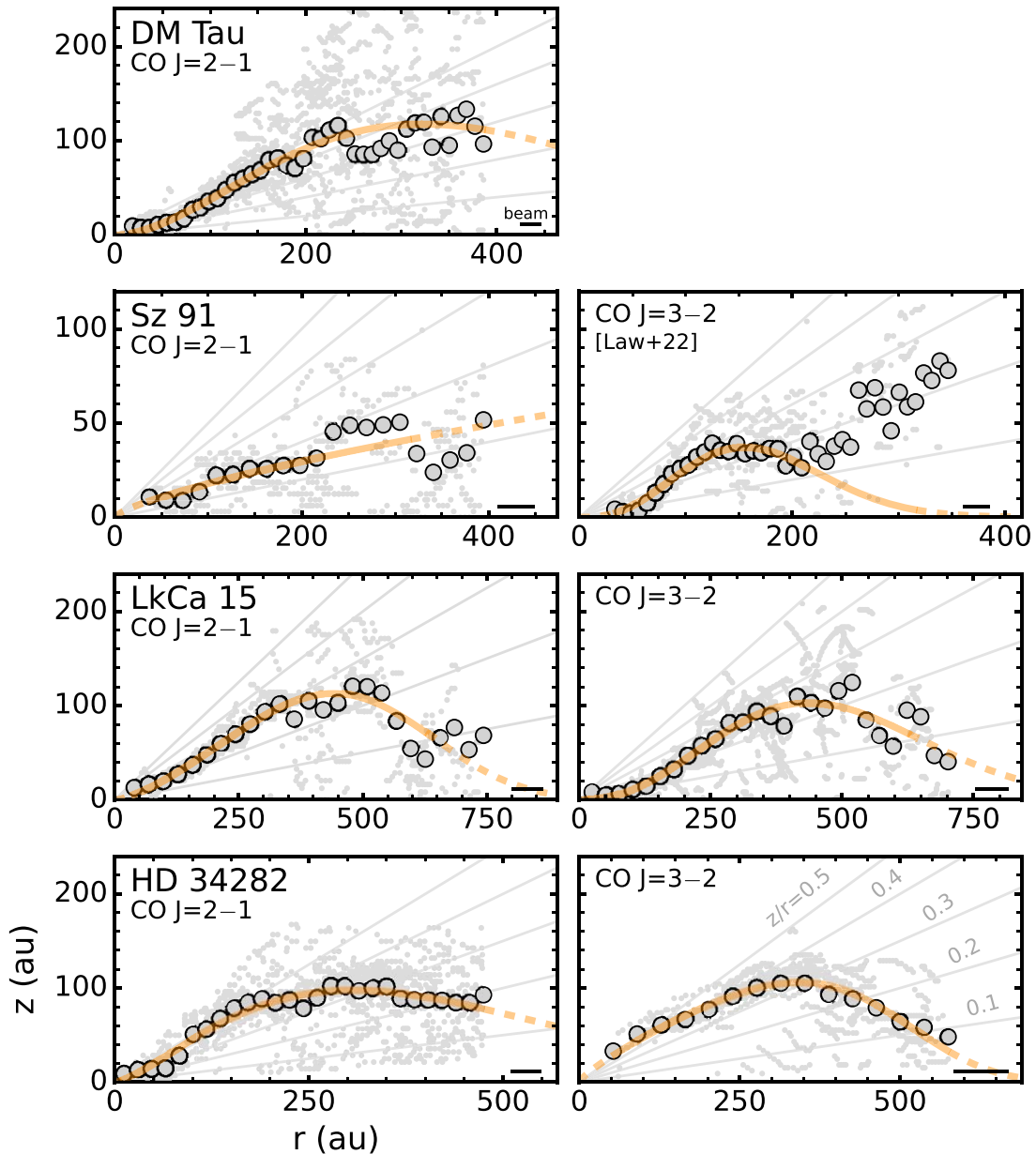
Figure 2. CO emission surfaces for the disks in our sample. Large gray points show radially binned surfaces and small, light gray points represent individual measurements. The CO $J = 3$–2 emission surface in the Sz 91 disk is taken from Law et al. (2022). The orange lines show the exponentially tapered power-law fits from Table 3, except for CO $J = 2$–1 in the Sz 91 disk, which shows a single power-law fit. The solid lines show the radial range used in the fitting, while the dashed lines are extrapolations. Lines of constant z/r from 0.1 to 0.5 are shown in gray. The FWHM of the major axis of the synthesized beam is shown in the bottom right corner of each panel.

(The data used to create this figure are available.)

uncertainties associated with fitting a functional form to the extracted data points and do not include the systematic uncertainties associated with extracting those data points (e.g., uncertainties in disk inclination and PA). We also list the maximum radius ($r_{\mathrm{fit, \, max}}$) that we considered for each surface fit.

4. Results

4.1. Overview of Emission Surfaces

Figures 2 and 3 show the CO and, when available, ^{13}CO emission surfaces, respectively, derived for the disks in our sample. In all cases, the CO surfaces lie at higher altitudes than

those of ^{13}CO, consistent with line optical depths of ~ 1 being reached at deeper layers for the less abundant ^{13}CO isotopologue. The inability to derive a ^{13}CO emission surface in the Sz 91 disk was driven by both low S/N and insufficient angular resolution, while for the HD 34282 disk, despite having the best angular resolution in our sample, the larger source distance prevented us from spatially resolving the ^{13}CO emitting heights. We do not resolve the vertical structure of the $C^{18}O$ emission in any disk, which suggests that $C^{18}O$ arises at or near the disk midplanes.

As shown in Figure 2, all disks show elevated CO emission with maximum absolute heights of ≈ 100 au, with the exception of the Sz 91 disk, which has CO heights of only ≈ 50 au. There
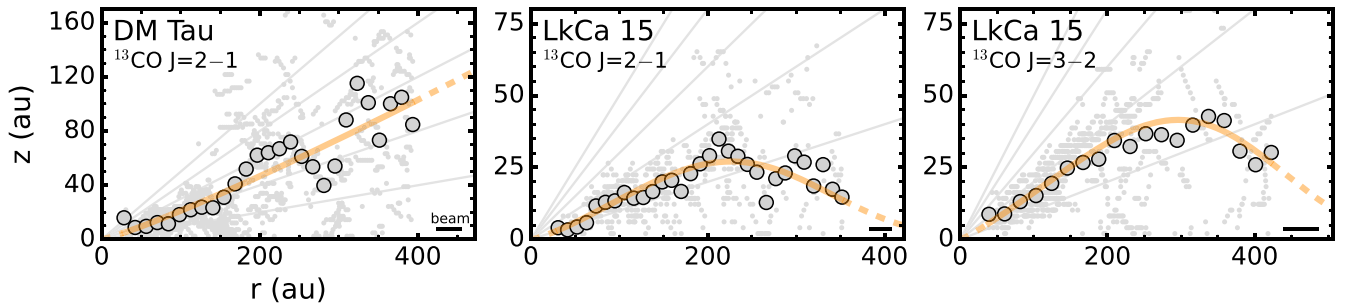
Figure 3. ^{13}CO emission surfaces in the DM Tau and LkCa 15 disks. The orange lines show the exponentially tapered power-law fits from Table 3, except for ^{13}CO $J = 2–1$ in the DM Tau disk, which shows a single power-law fit. Otherwise, as in Figure 3.

(The data used to create this figure are available.)

is considerable variation in the typical z/r values spanned by the surfaces from ≈ 0.1 to $\gtrsim 0.5$. The DM Tau disk has by far the most elevated CO emission surface, while Sz 91 hosts the flattest disk. Figure 3 shows that for those sources where we could derive ^{13}CO surfaces, the ^{13}CO surface traces between $z/r \gtrsim 0.2$ (DM Tau) and $z/r = 0.1$–0.15 (LkCa 15).

In all lines, the LkCa 15 disk shows the characteristic emission surface profile of a sharply rising surface in the inner disk, followed by a gradual flattening and then turnover at large radii which is, presumably, due to decreasing gas surface densities. The CO $J = 2–1$ surface in the DM Tau disk, and to a lesser degree the HD 34282 disk, does not clearly show a turnover at large radii and instead shows a prolonged plateau phase. The DM Tau disk is particularly reminiscent of the IM Lup disk, which showed similar diffuse, elevated CO emission at large radii (Pinte et al. 2018; Law et al. 2021a). The Sz 91 disk also does not show a clear turnover and instead appears to rise out to large radii, with a possible upturn at ≈ 400 au. This occurs at the radial location where we have insufficient S/N to be certain of this feature, but note that the more sensitive CO $J = 3–2$ data (Figure 2) show elevated, diffuse emission at similar radii (Tsukagoshi et al. 2019; Law et al. 2022).

To better illustrate the three-dimensional (3D) geometry of these line emission surfaces, we overlay the inferred CO emission surfaces on CO peak line intensity maps in Figure 4. All peak intensity maps were generated using the "quadratic" method of `bettermoments` with the full Planck function.

4.2. Radial Profiles and Substructures

In addition to the vertical structure, we also characterized the radial morphology of the CO isotopologue emission in each disk. We first generated a set of radial line intensity profiles (Section 4.2.1) and then used these profiles to catalog the properties of all substructures present in each source (Section 4.2.2) and to compute the radial size of the CO isotopologue line emission (Section 4.2.3).

4.2.1. Radial Line Intensity Profile Generation

We computed radial profiles using the `radial_profile` function in the `GoFish` python package (Teague 2019a) to deproject the zeroth moment maps. During deprojection, we incorporated the derived emission surfaces listed in Table 3. This is particularly important for highly elevated surfaces, e.g., CO, in order to derive accurate radial locations of line emission substructures (e.g., Law et al. 2021b; Rosotti et al. 2021). We

generated a set of radial profiles from azimuthally averaged profiles to those only including 15°, 30°, and 45° wedges along the disk major axis. Azimuthally averaged profiles are most sensitive to weaker emission at large radii, while profiles extracted from narrow wedges possess a higher effective spatial resolution, given adequate S/N. We chose profiles by visual inspection by prioritizing both the sharpness of substructures, which may otherwise be smoothed away in azimuthally averaged profiles, while maintaining profile fidelity for sources and lines with lower S/N. For the Sz 91 disk, we extracted the CO $J = 2–1$ radial profile in a $\pm 90°$ wedge in the northern part of the disk to avoid substantial cloud obscuration, following Law et al. (2022). Figure 5 shows the resultant radial profiles.

4.2.2. Radial Substructures

We used the radial profiles in Figure 5 to identify and catalog the properties of radial line emission substructures. We label each substructure according to established nomenclature (e.g., Huang et al. 2018a; Cieza et al. 2021; Law et al. 2021b), with local maxima denoted with "B" (for "bright") and local minima marked with "D" (for "dark") followed by their radial location rounded to the nearest astronomical unit. We colloquially refer to these features as rings and gaps, respectively. We catalog each feature closely following the methods of Law et al. (2021b), which, in short, is a combination of Gaussian profile decomposition, local extrema identification, and, when necessary, visual identification. All identified features are labeled in Figure 5 and cataloged in Table 4. We also identified rings and gaps present in the continuum emission profiles, but emphasize that this was done to ensure self-consistent comparisons, and the radial locations and widths derived from existing higher-angular-resolution observations often represent more accurate dust substructure properties; see, e.g., DM Tau (Kudo et al. 2018; Hashimoto et al. 2021), Sz 91 (Canovas et al. 2016; Maucó et al. 2021), HD 34282 (van der Plas et al. 2017), and LkCa 15 (Facchini et al. 2020).

Below, we briefly summarize the distribution of substructures for each of the disks in our sample.

DM Tau. Emission is sharply centrally peaked in all CO isotopologues with the majority of emission within ≈ 100 au, while diffuse, low-intensity emission extends to large disk radii. CO $J = 2–1$ emission is particularly extended, reaching as far as ~ 1000 au. Emission shoulders are present in ^{13}CO and C^{18}O between ~ 70 and 120 au and demarcate the transition between centrally peaked versus large-scale diffuse emission. We also identify a low-contrast C^{18}O emission shoulder around
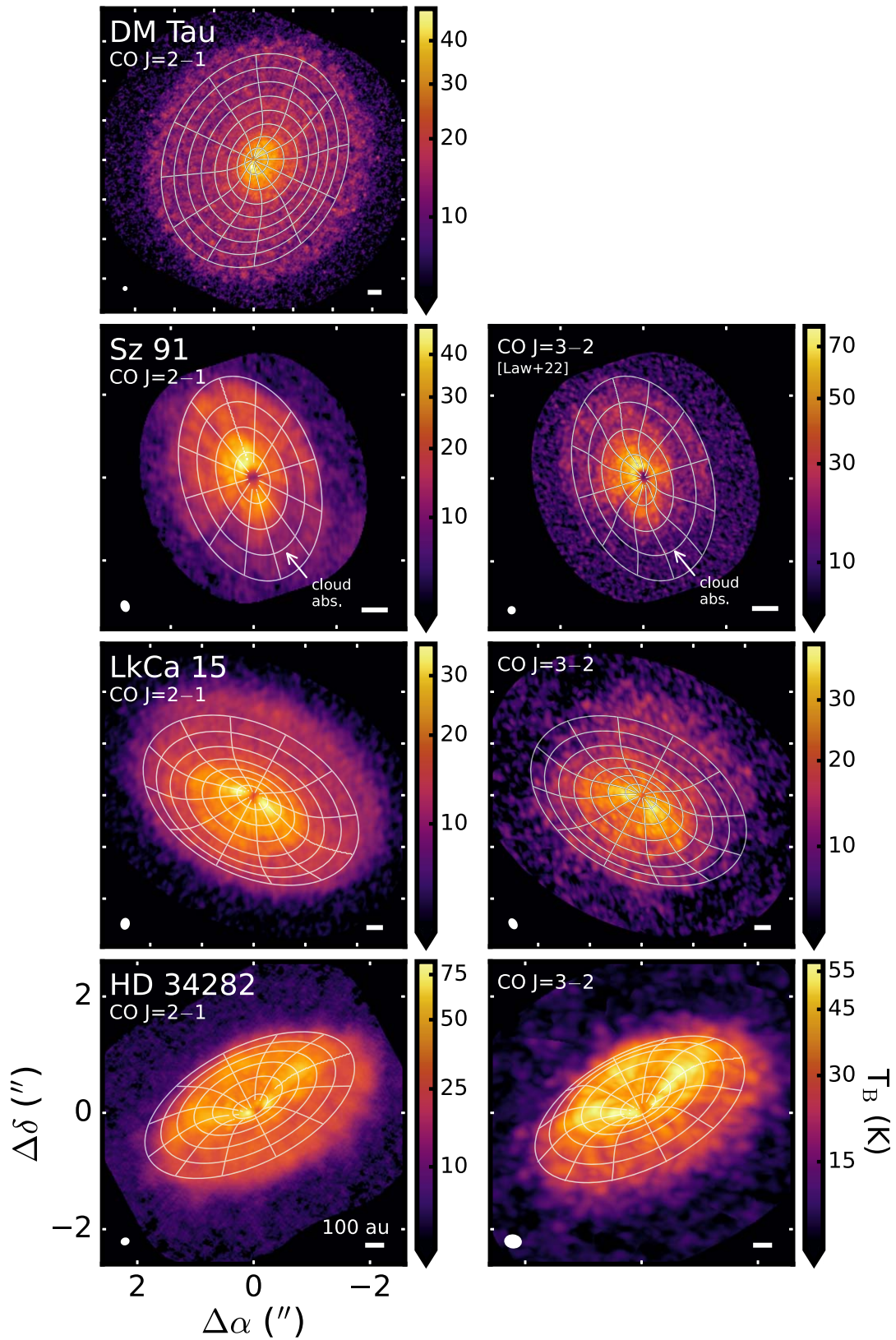
Figure 4. Peak intensity maps of CO $J = 2–1$ (left column) and, when available, $J = 3–2$ (right column), for those sources with directly extracted line emission surfaces. Overlaid contours show the fitted emission surfaces, as listed in Table 3. Panels for each disk have the same field of view, with each tick mark representing $2''$. The CO $J = 3–2$ surface in the Sz 91 disk is taken from Law et al. (2022). The synthesized beam and a scale bar indicating 100 au is shown in the lower left and lower right corners, respectively, of each panel.

40 au, which suggests that the inner disk hosts additional small-scale substructures which are not clearly resolved at the current beam sizes ($0''12–0''20$; 17–30 au).

Sz 91. All CO isotopologues show a consistent radial morphology in the form of a central dip or hole, a single wide ring at ≈60–70 au, and diffuse emission out to ∼300–400 au.
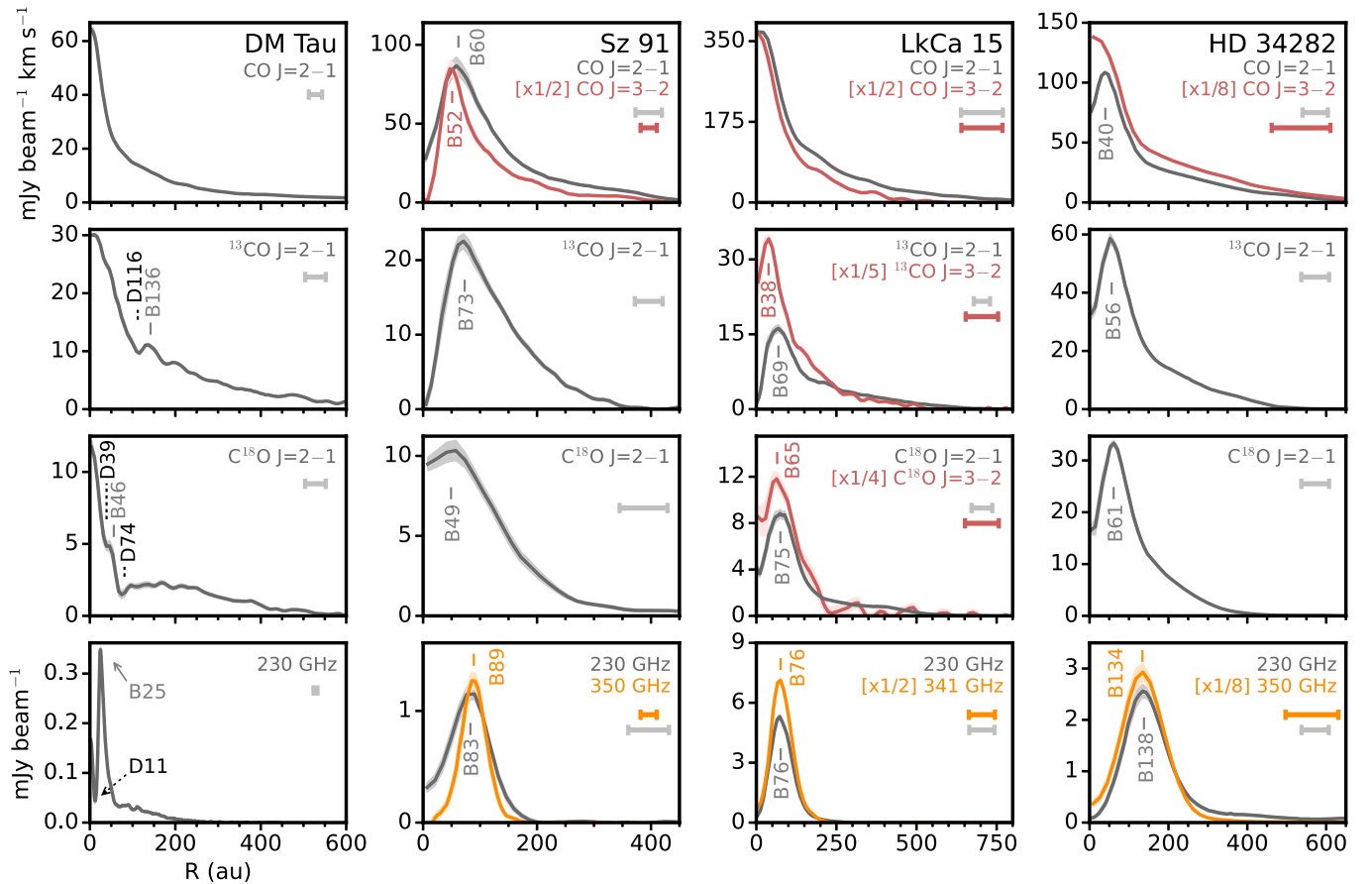
Figure 5. Deprojected radial intensity profiles of CO, ^{13}CO, and C^{18}O lines, and the continuum (from top to bottom). Shaded regions show the 1σ scatter at each radial bin (i.e., arc or annulus) divided by the square root of the ratio of bin circumference and FWHM of the synthesized beam. Solid lines mark rings and dotted lines mark gaps. When available, radial profiles of other lines from the same CO isotopologue are shown in dark red, while those from additional continuum frequencies are colored in orange. Occasionally, line intensities are scaled down by a constant factor for visual clarity. Diffuse, large-scale CO $J = 2-1$ emission in the DM Tau disk is truncated for better comparison with other lines but extends to $\gtrsim 1000$ au. The CO $J = 3-2$ and 350 GHz continuum radial profiles of the Sz 91 disk are taken from Tsukagoshi et al. (2019) and Law et al. (2022). The FWHM of the synthesized beam is shown by a horizontal bar in the upper right corner of each panel.

This ring structure is now clearly confirmed by the distribution of the ^{13}CO $J = 2-1$ emission, as previous observations in CO lines suffered from potential confusion due to cloud obscuration (e.g., Canovas et al. 2015; Tsukagoshi et al. 2019).

LkCa 15. CO emission appears centrally peaked with diffuse emission extending to large radii ($\sim$500–700 au), while the ^{13}CO and C^{18}O isotopologues show emission in the form of a ring at 40–70 au and a central dip/hole is resolved. The presence of this central dip and ring was hinted at in the previous observations of the $J = 3-2$ line (Jin et al. 2019), but is clearly confirmed in the higher-angular-resolution $J = 2-1$ data.

HD 34282. The radial distribution of CO isotopologue emission in the HD 34282 disk is quite similar to that of Sz 91: a central dip, a single ring around 40–60 au, and diffuse emission out to $\sim$350–600 au. We also note that this is the only source in our sample that shows a prominent asymmetry in its millimeter continuum emission (see, e.g., van der Plas et al. 2017; Figure 1). No such asymmetries are evident in the line emission.

Line emission peaks are approximately radially coincident with the continuum emission ring in the DM Tau and LkCa 15 disks, while the Sz 91 and HD 34282 disks show either small ($\approx$10–30 au) or large ($\approx$80–100 au) offsets, respectively, with their CO line emission rings located interior to the continuum peaks.

4.2.3. Gas Disk Sizes

We also computed the radial sizes of the CO isotopologue lines by determining the radius in which 90% of the total flux is contained (e.g., Tripathi et al. 2017; Ansdell et al. 2018; Long et al. 2022). We also determined the outermost edge of the emission defined by the radius containing 99% of the flux, which is an important metric for disks showing very extended but low-intensity emission, such as the DM Tau disk. Table 5 lists the computed disk sizes for all CO isotopologue lines and for the continuum. For all sources, the CO emission shows the largest radial extent, followed by ^{13}CO and then C^{18}O, with the exception of C^{18}O in the Sz 91 disk. However, this large C^{18}O size in this disk likely reflects the larger beam due to substantial uv-tapering, so we urge caution in interpreting this value. The ratio of the radial extents of the line emission versus that of the continuum varies substantially in the disks in our sample, with, for instance, the DM Tau and LkCa 15 disks having CO disk sizes that are nearly 4–5 times that of the millimeter continuum, while the radial extent of the CO emission in the HD 34282 disk is approximately twice that of the continuum.

4.3. Comparison of $J = 2-1$ and $J = 3-2$ Emission Surfaces

For several sources, we have CO isotopologue emission surfaces for both the $J = 2-1$ and $J = 3-2$ lines, either derived directly in this work as for the HD 34282 and LkCa 15 disks or

Table 4
Properties of Radial Substructures

Source (1)	Line (2)	Feature (3)	r_0 (mas) (4)	r_0 (au) (5)	Method (6)	Width (au) (7)
DM Tau	$^{13}CO\ J = 2-1$	D116	810.9 ± 49.1	116.0 ± 7.0	R	17.2 ± 0.2
	$^{13}CO\ J = 2-1$	B136	950.0 ± 5.4	135.9 ± 0.8	G	85.2 ± 1.6
	$C^{18}O\ J = 2-1$	D39	272.5 ± 49.5	39.0 ± 7.1	V	...
	$C^{18}O\ J = 2-1$	B46	321.4 ± 49.5	46.0 ± 7.1	V	...
	$C^{18}O\ J = 2-1$	D74	519.5 ± 49.5	74.3 ± 7.1	R	~ 30
	230 GHz, cont.	D11	76.9 ± 9.4	11.0 ± 1.3	V	...
	230 GHz, cont.	B25	175.5 ± 0.5	25.1 ± 0.1	G	13.7 ± 0.6
Sz 91	$CO\ J = 2-1$	B60	382.3 ± 4.9	60.4 ± 0.8	G	90.2 ± 1.4
	$^{13}CO\ J = 2-1$	B73	461.6 ± 4.1	72.9 ± 0.6	G	89.8 ± 5.6
	$C^{18}O\ J = 2-1$	B49	307.4 ± 3.2	48.5 ± 0.5	G	174.9 ± 3.5
	$CO\ J = 3-2$[a]	B52	327.4 ± 1.9	51.7 ± 0.3	G	58.4 ± 10.1
	230 GHz, cont.	B83	522.7 ± 6.4	82.5 ± 1.0	G	82.4 ± 2.0
	350 GHz, cont.[a]	B89	562.1 ± 1.0	88.7 ± 0.2	G	52.8 ± 3.4
LkCa 15	$^{13}CO\ J = 2-1$	B69	439.9 ± 12.1	68.8 ± 1.9	G	109.3 ± 3.5
	$C^{18}O\ J = 2-1$	B75	481.3 ± 9.0	75.3 ± 1.4	G	116.5 ± 2.5
	$^{13}CO\ J = 3-2$	B38	240.0 ± 17.6	37.6 ± 2.8	G	91.1 ± 9.7
	$C^{18}O\ J = 3-2$	B65	415.6 ± 24.9	65.0 ± 3.9	G	123.8 ± 19.4
	230 GHz, cont.	B76	484.0 ± 3.8	75.8 ± 0.6	G	80.1 ± 0.7
	341 GHz, cont.	B76	486.2 ± 2.5	76.1 ± 0.4	G	75.0 ± 1.8
HD 34282	$CO\ J = 2-1$	B40	130.7 ± 1.9	40.0 ± 0.6	G	101.1 ± 3.7
	$^{13}CO\ J = 2-1$	B56	181.9 ± 2.4	55.7 ± 0.7	G	97.2 ± 2.5
	$C^{18}O\ J = 2-1$	B61	200.5 ± 3.0	61.4 ± 0.9	G	96.1 ± 5.0
	230 GHz, cont.	B138	451.2 ± 6.3	138.2 ± 1.9	G	123.2 ± 0.6
	350 GHz, cont.	B134	437.7 ± 6.5	134.1 ± 2.0	G	127.4 ± 0.2

Notes. Column descriptions: (1) Name of host star. (2) Name of line. (3) Substructure label. B (bright) prefix refers to rings and D (dark) refers to gaps. (4) Radial location of substructure in millarcseconds. (5) Radial location of substructure in astronomical units. (6) Method used to derive radial location of substructure: "G" indicates Gaussian fitting, "R" indicates identification of local extrema in radial profiles, and "V" indicates identification through visual inspection. (7) Width of substructure. Uncertainties on the radial locations and widths represent Gaussian fitting errors for "G" features. Positional uncertainties for "R" or "V" features are estimated as the width of one radial bin in the associated radial profile, while the widths of "R" features are computed following the procedure of Huang et al. (2018a). All uncertainties are 1σ.
[a] Radial profile taken from Tsukagoshi et al. (2019) and Law et al. (2022).

by combining our results with those in the literature. CO rotational lines with sufficiently different excitation properties are expected to probe distinct regions within a disk, due to changing excitation conditions combined with strong radial and vertical temperature gradients across disks (e.g., Dartois et al. 2003; Bruderer et al. 2012; Fedele et al. 2016). We can now directly assess if any such excitation-related effects, i.e., differing emission heights between lines, are present in a small sample of disks.

Figure 6 shows those sources where we have emission surfaces of both the $J = 2-1$ and $J = 3-2$ lines in either CO and/or ^{13}CO. In this sample, we also included the HD 163296 and GM Aur disks, which have CO and ^{13}CO $J = 2-1$ surfaces, respectively, derived as part of the MAPS program (Law et al. 2021a), as well as ^{13}CO $J = 3-2$ in GM Aur (Schwarz et al. 2021). We also extracted the CO $J = 3-2$ surface of HD 163296 from ALMA science verification data (e.g., Rosenfeld et al. 2013; de Gregorio-Monsalvo et al. 2013) using the same methods described in Section 3.1. While the ALMA science verification data of CO $J = 3-2$ in the HD 163296 disk and the ^{13}CO $J = 3-2$ data in the GM Aur disk have considerably coarser beams than used in this work, we do not expect these larger beam sizes to significantly influence the derived surfaces for these disks (see Appendix D in Law et al. 2021a).

In all disks and in either CO or ^{13}CO, the $J = 3-2$ and $J = 2-1$ lines show consistent line emission heights. In a few cases, there are hints that the $J = 3-2$ surface is more elevated than that of the $J = 2-1$, particularly at large radii. This is most notable in the ^{13}CO emission surfaces of the GM Aur disk and, to a lesser degree, in the LkCa 15 disk, but in neither case do we consider these putative differences conclusive. The overall similarity in line emission heights is perhaps not surprising, given that these surfaces are derived from consecutive low-J lines that span a relatively narrow range in excitation conditions, i.e., the upper-state energy of the CO $J = 3-2$ line ($E_u \approx 33.2$ K) is only twice that of the $J = 2-1$ line ($E_u \approx 16.6$ K). This is consistent with the traditional assumption that low ($J_u < 6$) CO rotational lines are tracing the cold gas in the outer disk. Thus, as the line emission is originating from similar heights, we expect both lines to be tracing gas at approximately the same temperature in each disk. We return to this in more detail in Section 4.5.

4.4. Comparison with Near-IR Scattering Surfaces

The vertical distribution of micron-sized dust grains in disks should be largely correlated with the vertical gas structure as small dust grains are expected to be strongly coupled to the gas. A detailed understanding of this relationship is critical, as dust evolution from micron-sized grains to pebbles is an important step in the planet formation process. Here, we compare
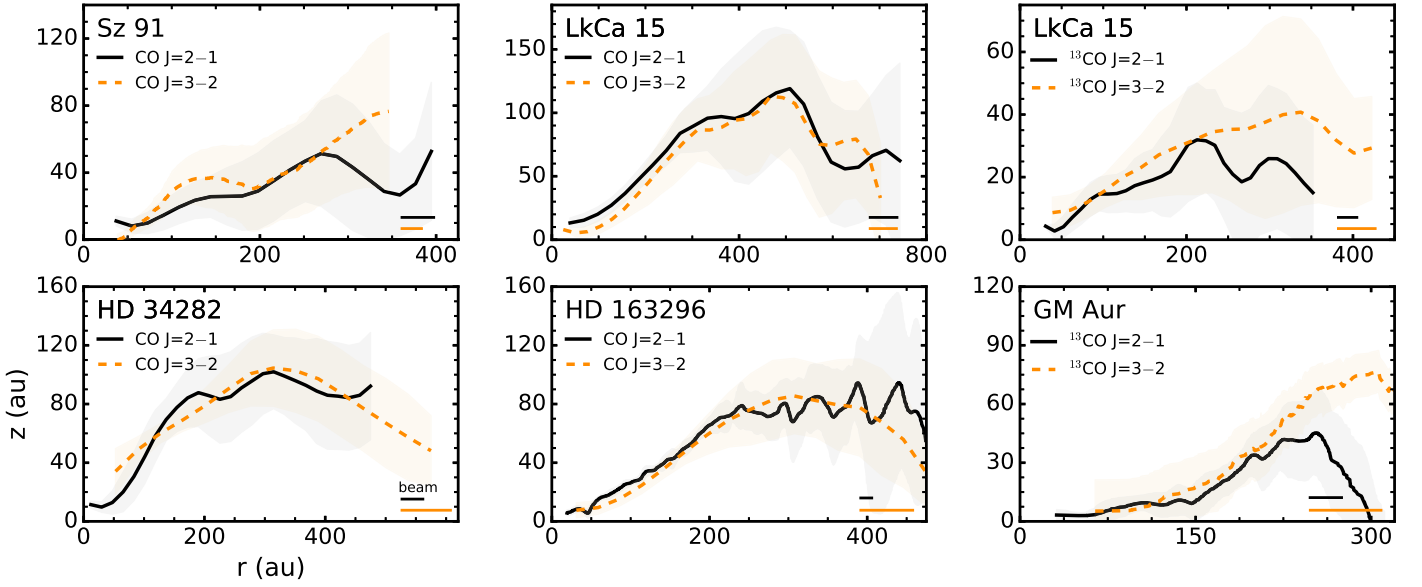
Figure 6. Comparison of CO and ^{13}CO emission surfaces in the $J = 2$–1 and $J = 3$–2 lines, which are shown as solid black and dashed orange lines, respectively. The lines are the moving average surfaces and shaded regions show the 1σ uncertainty. The FWHM of the major axis of the synthesized beam is shown the bottom right corner panel. The HD 163296 CO $J = 3$–2 surface was derived from ALMA science verification data (e.g., de Gregorio-Monsalvo et al. 2013; Rosenfeld et al. 2013), as described in Section 4.3. The other surfaces are taken from CO $J = 3$–2 in Sz 91 (Law et al. 2022), ^{13}CO $J = 3$–2 in GM Aur (Schwarz et al. 2021), and CO and ^{13}CO $J = 2$–1 in HD 163296 and GM Aur, respectively (Law et al. 2021a).

Table 5
Gas Disk Sizes

Source	Line	R_{size} (au)	R_{edge} (au)
DM Tau	CO $J = 2$–1	817 ± 5	977 ± 7
	^{13}CO $J = 2$–1	577 ± 15	768 ± 19
	C^{18}O $J = 2$–1	473 ± 23	620 ± 17
	230 GHz cont.	204 ± 13	281 ± 18
Sz 91	CO $J = 2$–1	368 ± 9	502 ± 17
	^{13}CO $J = 2$–1	275 ± 18	464 ± 78
	C^{18}O $J = 2$–1	397 ± 29	579 ± 22
	230 GHz cont.	135 ± 15	176 ± 61
	350 GHz cont.	123 ± 6	159 ± 10
LkCa 15	CO $J = 2$–1	730 ± 15	971 ± 19
	^{13}CO $J = 2$–1	526 ± 11	690 ± 32
	C^{18}O $J = 2$–1	457 ± 9	622 ± 29
	CO $J = 3$–2	560 ± 57	810 ± 29
	^{13}CO $J = 3$–2	432 ± 26	556 ± 25
	C^{18}O $J = 3$–2	191 ± 27	276 ± 28
	230 GHz cont.	153 ± 9	235 ± 10
	341 GHz cont.	142 ± 9	194 ± 9
HD 34282	CO $J = 2$–1	599 ± 9	843 ± 12
	^{13}CO $J = 2$–1	428 ± 10	631 ± 27
	C^{18}O $J = 2$–1	338 ± 11	541 ± 30
	CO $J = 3$–2	622 ± 20	861 ± 27
	230 GHz cont.	294 ± 10	376 ± 9
	350 GHz cont.	239 ± 18	483 ± 32

Note. Disk size (R_{size}) and outer edge (R_{edge}) were computed as the radius which encloses 90% and 99% of the total disk flux, respectively. Uncertainties do not include the effect of differing beam sizes.

observations of line emission surfaces with scattering heights measured in the near-IR (NIR; e.g., Ginski et al. 2016; Monnier et al. 2017; Avenhaus et al. 2018; Garufi et al. 2020).

Both the HD 34282 (de Boer et al. 2021; Quiroz et al. 2022) and LkCa 15 (Thalmann et al. 2015, 2016; Oh et al. 2016; Currie et al. 2019) disks have existing NIR polarimetric

imaging that show well-defined rings, from which direct estimates of the small dust scattering heights can be inferred.[23] The NIR heights of the rings in the HD 34282 disk were derived by de Boer et al. (2021), but, to our knowledge, no such heights have been reported for the LkCa 15 disk. Instead, we estimated the scattering height of the outer NIR ring in the LkCa 15 disk from the existing SPHERE images of Thalmann et al. (2016), following the procedures outline in Rich et al. (2021) and described in detail in Appendix C. We do not attempt to derive a scattering height for the inner disk ($\lesssim$30 au) component.

Figure 7 shows these NIR heights compared to the CO isotopologue line emission surfaces derived in this work. In both the LkCa 15 and HD 34282 disks, the NIR ring heights lie at approximately the same height as the CO line emission surfaces. In general, but not exclusively, the scattering surfaces in disks have been found to lie lower than the CO surface and are instead often approximately vertically colocated with ^{13}CO line emitting heights (Law et al. 2021a, 2022; Rich et al. 2021). NIR rings within 100 au, however, such as in the HD 163296 disk (Law et al. 2021a; Rich et al. 2021), are located at nearly the same height as CO, which is similar to what is observed here in both the LkCa 15 and HD 34282 disks.

Overall, these results suggest an unexplored diversity in the relative distributions of small dust scattering surfaces and line emitting layers in disks. Comparisons between directly mapped line emission surfaces in disks with known scattering heights provide a powerful empirical way to probe multiple disk components at the same time, especially in light of the growing number of high-angular-resolution ALMA observations of CO isotopologue emission lines in those disks with known NIR features.

---

[23] After applying a height-corrected deprojection, de Boer et al. (2021) find that the outer ring is also consistent with a single-armed spiral rather than a circular ring, while Marr & Dong (2022) suggest this feature may instead be a vortex.
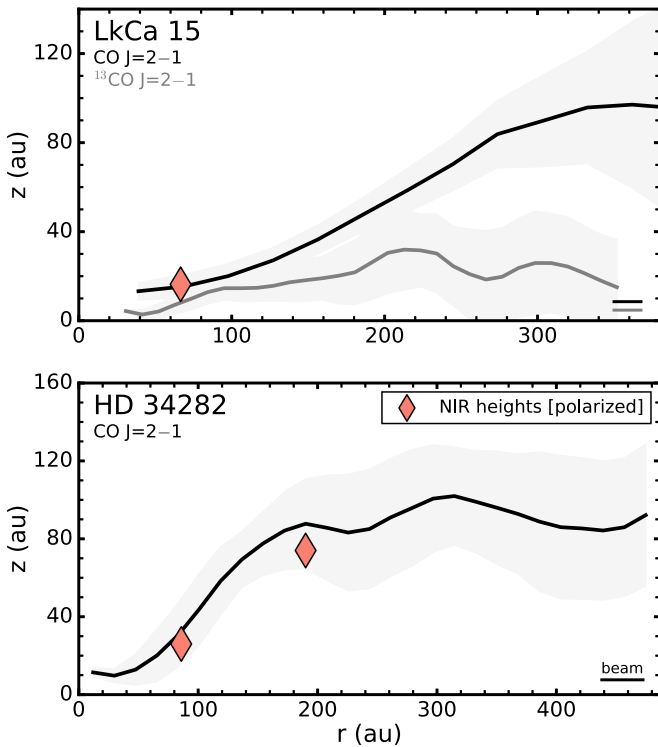
Figure 7. CO and, when available, ^{13}CO emission surfaces for the LkCa 15 and HD 34282 disks vs. NIR heights. The lines are the moving average surfaces and gray shaded regions show the 1σ uncertainty. The red markers show individual height measurements from polarimetric imaging from NIR rings in the HD 34282 disk (de Boer et al. 2021). The NIR ring height for the LkCa 15 disk is derived in Appendix C. Uncertainties are smaller than the markers, but are on the order of a few astronomical units. The FWHM of the major axis of the synthesized beam is shown in the bottom right corner of each panel.

4.5. Disk Thermal Structure

4.5.1. Calculating Gas Temperatures

The peak surface brightness, I_ν, of optically thick, spatially resolved emission that fills the beam and is in local thermodynamic equilibrium provides a measure of local gas temperature. At typical temperatures and densities in protoplanetary disks, CO and ^{13}CO line emission are expected to be optically thick (e.g., Weaver et al. 2018), and we can use this emission to compute their temperature structure.

To extract gas temperatures, we closely followed the procedures of Law et al. (2021a). We repeated the surface extractions as in Section 3.1 on the non-continuum-subtracted image cubes, which ensures that we do not underestimate the line intensity along lines of sight containing strong continuum emission (e.g., Boehler et al. 2017). We then converted the peak surface brightness I_ν of each extracted pixel to a brightness temperature using the full Planck function and assume the resulting brightness temperature is equal to the local gas temperature. Since the CO $J = 2–1$ emission in the Sz 91 disk suffers from moderate cloud contamination, we manually excluded the affected channels ($\approx$4–7 km s^{-1}) when extracting line emission heights.

4.5.2. Radial Temperature Profiles

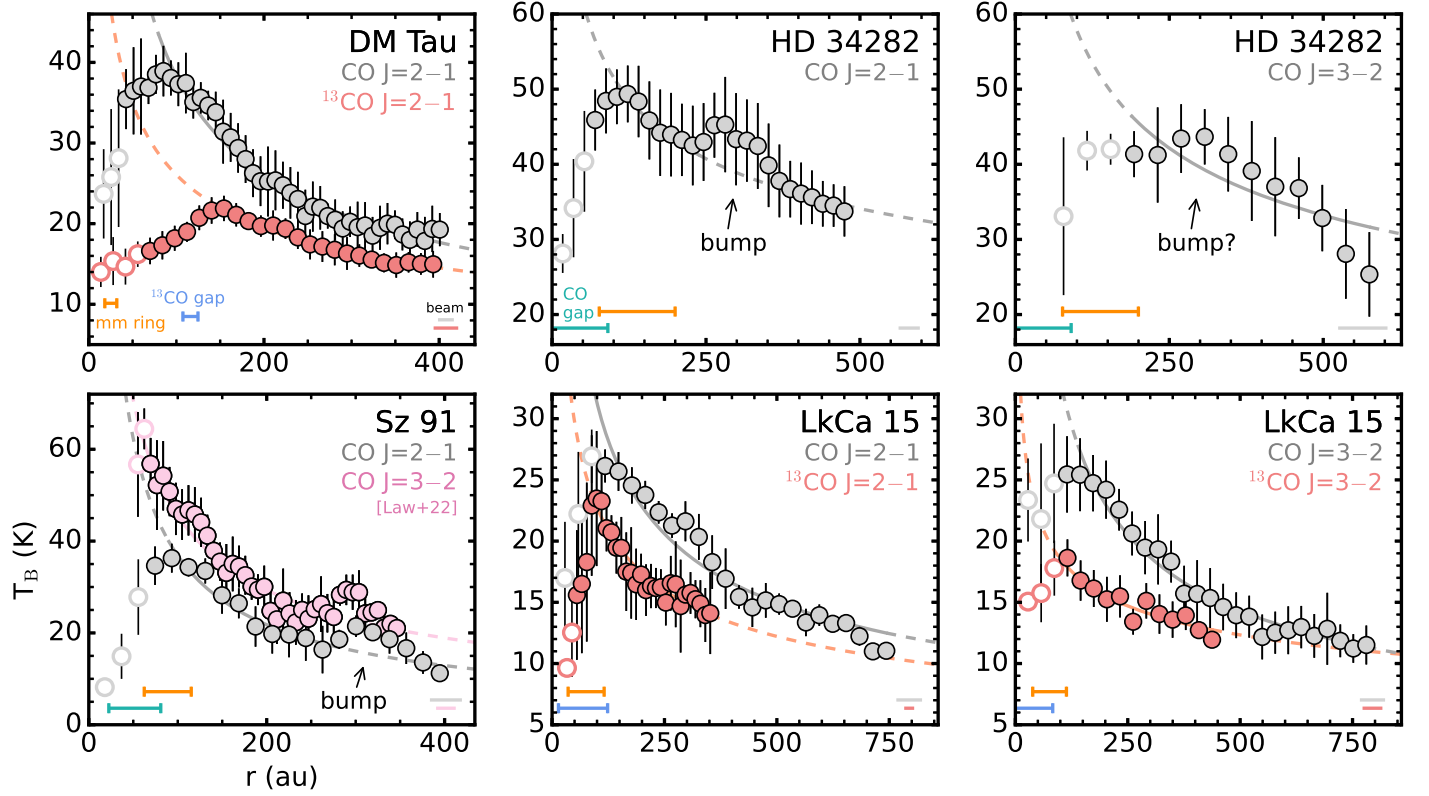Figure 8 shows the CO and, when available, ^{13}CO radial temperature distributions along the emission surfaces. Derived brightness temperatures are generally consistent with expectations based on stellar luminosity and spectral classes, with the disk around Herbig Ae star HD 34282 showing warmer temperatures than those around the T Tauri stars.

Many sources show drops in brightness temperatures toward their inner disks, as seen in Figure 8. At the smallest radii, this is primarily due to beam dilution as the emitting area becomes comparable to or smaller than the angular resolution of the observations. For instance, in the Sz 91 disk, the higher-angular-resolution CO $J = 3–2$ observations show an increasing temperature profile toward the inner disk, which indicates that the observed turnover at $\sim$100 au in the CO $J = 2–1$ temperature profile is primarily a beam effect. However, some sources show flattening or declining temperature profiles (toward the central star) at radii beyond that of the beam size. There are several possible explanations, e.g., CO gas depletion, dust absorption, or unresolved CO emission substructure. The dip in CO temperatures in the DM Tau disk is likely, at least in part, due to dust optical depth, since the ring at $\sim$20 au shows $\tau \gtrsim 1$ (Hashimoto et al. 2021), while it is not clear what is driving the sharp change in the ^{13}CO gas temperature. The inner disk of LkCa 15 shows marginally optically thick ($\tau \sim 0.5$) dust (Facchini et al. 2020) and decreased gas column density (Leemker et al. 2022), which both likely contribute to the observed temperature drops in Figure 8.

Beyond these inner dips, the radial temperature profiles are generally smooth, with a few exceptions. We identify a local temperature bump in the CO $J = 2–1$ temperatures of both the Sz 91 and HD 34282 disks. The feature in the HD 34282 disk is located at a radius of $\approx$280 au, while the enhancement in the Sz 91 disk occurs at approximately 310 au, which is coincident with a similar enhancement at $\approx$300 au seen in the CO $J = 3–2$ temperature profile (Law et al. 2022). Both features have relatively broad widths of $\approx$125–150 au and are listed in Table 6. A tentative bump is also seen at 300 au in the CO $J = 3–2$ line in the HD 34282 disk, which is consistent with the location of the enhancement in the $J = 2–1$ line. However, due to the larger beam size, it is difficult to confirm the reality of this feature.

In most outer disk regions, the gas temperatures drop below the CO freeze-out temperature, indicating that our approach breaks down as we approach the low-density, partially optically thin outer disk.

The temperatures that we derive agree well with previous estimates in the same disks. The CO gas temperatures of the DM Tau disk are consistent with those inferred using previous lower-angular-resolution ($\gtrsim$0″3) CO $J = 2–1$ observations (Flaherty et al. 2020; Law et al. 2022), with peak gas temperatures inferred here being only 2–3 K greater than those seen previously. The CO and ^{13}CO gas temperatures in the inner 200 au of the LkCa 15 disk, which were estimated using observations at $\approx$0″3 (Leemker et al. 2022), are a few kelvins warmer, but are generally consistent, with our estimates. The Sz 91 disk has a steep temperature profile in the inner disk, which was derived in the same way using CO $J = 3–2$ observations at 0″14 (Law et al. 2022) and, for comparison, we also show this temperature in Figure 8. Although the angular resolution of the CO $J = 2–1$ data used here is only $\approx$1.5 times larger that of the CO $J = 3–2$ data, we are not sensitive to warm gas in the inner 100 au due to beam dilution. For instance, gas temperatures derived from CO $J = 3–2$ observations are nearly 70 K at $\approx$50 au (Law et al. 2022). We also note that, at any

Figure 8. CO and, when available, ^{13}CO radial brightness temperature profiles. These profiles represent the mean temperatures computed by radially binning the individual measurements, similar to the procedure used to compute the radially binned surfaces (see Section 4.5). Vertical lines show the 1σ uncertainty, given as the standard deviation of the individual measurements in each bin. The solid gray lines show the power fits from Table 6, while the dashed lines are extrapolations. Temperature measurements with radii less than 2 times the beam major axis FWHM are shown as hollow markers and are not used in the power-law fits. Orange error bars represent millimeter dust rings, while light green and blue error bars show CO and ^{13}CO line emission gaps, respectively. The FWHM of the major axis of the synthesized beam is shown in the bottom right corner of each panel.

Table 6
Radial Temperature Profile Fits

Source	Line	$r_{\mathrm{fit,in}}$ (au)	$r_{\mathrm{fit,out}}$ (au)	T_{100} (K)	q	Feat.[a]
DM Tau	CO $J = 2-1$	80	401	38 ± 0.5	0.56 ± 0.02	...
	^{13}CO $J = 2-1$	140	393	26 ± 0.4	0.42 ± 0.02	...
Sz 91	CO $J = 2-1$[b]	90	270	37 ± 1.2	0.76 ± 0.07	B310
	CO $J = 3-2$[b,c]	69	250	47 ± 0.7	0.70 ± 0.03	B300
LkCa 15	CO $J = 2-1$	90	743	31 ± 1.0	0.46 ± 0.03	...
	^{13}CO $J = 2-1$	98	352	23 ± 0.4	0.39 ± 0.02	...
	CO $J = 3-2$	140	781	33 ± 0.8	0.52 ± 0.02	...
	^{13}CO $J = 3-2$	116	437	19 ± 0.7	0.25 ± 0.04	...
HD 34282	CO $J = 2-1$[b]	105	238	52 ± 0.5	0.26 ± 0.01	B280
	CO $J = 3-2$[b]	190	575	58 ± 6.6	0.34 ± 0.09	B300

Notes.
[a] Local temperature bumps (B) are labeled according to their approximate radial location in astronomical units.
[b] Temperature bumps in the Sz 91 and HD 34282 disks are excluded in the power-law fits.
[c] Temperature fit is from Law et al. (2022).

particular radius, the CO $J = 2-1$ temperature is 5–8 K lower than that of the $J = 3-2$ profile, which, unlike in the DM Tau disk, suggests that the temperatures derived here are being modestly lowered by nonunity beam filling factors. While it is possible that in the Sz 91 disk the lower CO $J = 2-1$ temperatures relative to the $J = 3-2$ line may instead reflect an origin of the $J = 2-1$ line in colder disk material, this is unlikely given the similar emitting heights of both lines (Figure 6).

We fitted all temperature profiles with power-law profiles, parameterized by slope q and T_{100}, the brightness temperature at 100 au, i.e.,

$$T = T_{100} \times \left(\frac{r}{100 \text{ au}}\right)^{-q}. \qquad (2)$$

We excluded all temperatures within 2 times the FWHM of the major axis of the synthesized beam as these are likely affected by beam dilution, as discussed above. We also
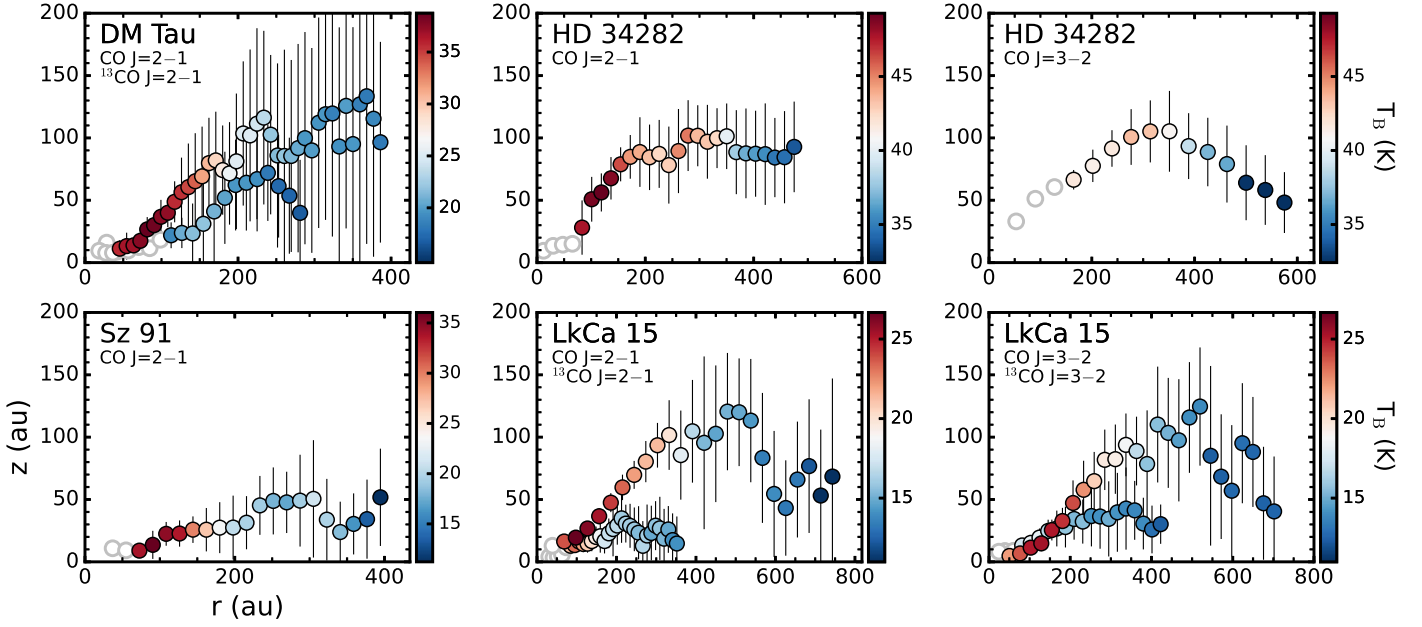
Figure 9. Two-dimensional (2D) temperature distributions of CO and, when available, ^{13}CO emission surfaces in all disks. Points are those from the binned surfaces and error bars are the 1σ uncertainties in z. Temperature measurements with radii less than 2 times the beam major axis FWHM are marked by hollow markers. The diffuse ^{13}CO emission at large radii in the DM Tau disk is not shown due to its low S/N and high scatter. For some of the innermost points, the uncertainty is smaller than the marker. The uncertainty of the temperature measurements, which is not shown here, can be seen in Figure 8.

(The data used to create this figure are available.)

Table 7
Summary of 2D Temperature Structure Fits

Source	$T_{\mathrm{atm},0}$ (K)	$T_{\mathrm{mid},0}$ (K)	q_{atm}	q_{mid}	z_0 (au)	α	β
DM Tau	$38^{+0.5}_{-0.4}$	$26^{+0.3}_{-0.4}$	$-0.74^{+0.02}_{-0.02}$	$-0.39^{+0.02}_{-0.01}$	$18^{+1.0}_{-0.9}$	$2.14^{+0.09}_{-0.09}$	$-0.07^{+0.05}_{-0.05}$
LkCa 15	$35^{+0.9}_{-0.9}$	$21^{+0.3}_{-0.3}$	$-0.59^{+0.03}_{-0.03}$	$-0.29^{+0.01}_{-0.01}$	$17^{+1.5}_{-1.5}$	$2.57^{+0.22}_{-0.2}$	$0.10^{+0.04}_{-0.04}$

excluded the temperature bumps in both the Sz 91 (> 270 au) and HD 34282 ($\approx$240–380 au) disks. Each profile was then fit using the Levenberg–Marquardt minimization implementation in `scipy.optimize.curve_fit`. Table 6 lists the fitting ranges and derived parameters. Most sources are fit well by power-law profiles with $q \approx 0.4$–0.6, with CO $J = 2$–1, 3–2 in HD 34282 and ^{13}CO $J = 3$–2 being considerably shallower ($q \approx 0.25$). The Sz 91 disk shows the steepest profile with $q = 0.76$, which is consistent with the similarly steep CO $J = 3$–2 profile ($q = 0.70$) found in Law et al. (2022).

4.5.3. Two-dimensional Temperature Profiles

Combining all line data for each source, Figure 9 shows the thermal structure of the CO and, when available, ^{13}CO emitting layers as a function of (r, z) for each source.

For those sources where we have multiple CO isotopologue surfaces, which trace different heights in the same disk, we can construct a two-dimensional (2D) model of the temperature distribution. We adopt the same two-layer model used in Law et al. (2021a), which is similar to the one proposed by Dartois et al. (2003), and then subsequently modified with a different connecting term by Dullemond et al. (2020).

The midplane temperature, T_{mid}, and atmosphere temperature, T_{atm}, are assumed to have a power-law profile with

slopes q_{mid} and q_{atm}, respectively:

$$T_{\mathrm{mid}}(r) = T_{\mathrm{mid},0}(r/100 \text{ au})^{q_{\mathrm{mid}}}, \quad (3)$$

$$T_{\mathrm{atm}}(r) = T_{\mathrm{atm},0}(r/100 \text{ au})^{q_{\mathrm{atm}}}. \quad (4)$$

Between the disk midplane and atmosphere, the temperature is smoothly connected using a tangent hyperbolic function:

$$T^4(r, z) = T_{\mathrm{mid}}^4(r) + \frac{1}{2}\left[1 + \tanh\left(\frac{z - \alpha z_q(r)}{z_q(r)}\right)\right]T_{\mathrm{atm}}^4(r), \quad (5)$$

where $z_q(r) = z_0(r/100 \text{ au})^{\beta}$. The α parameter defines the height at which the transition in the tanh vertical temperature profile occurs, while β describes how the transition height varies with radius.

We fit the individual, per-pixel temperature measurements of CO and ^{13}CO using `emcee` (Foreman-Mackey et al. 2013) to estimate the following seven parameters: $T_{\mathrm{atm},0}$, q_{atm}, $T_{\mathrm{mid},0}$, q_{mid}, α, z_0, and β. We used 256 walkers, which take 500 steps to burn in, and then an additional 5000 steps to sample the posterior distribution function. We took parameter values and uncertainties as the 50th, 16th, and 84th percentiles from the marginalized posterior distributions, respectively, and list them in Table 7.
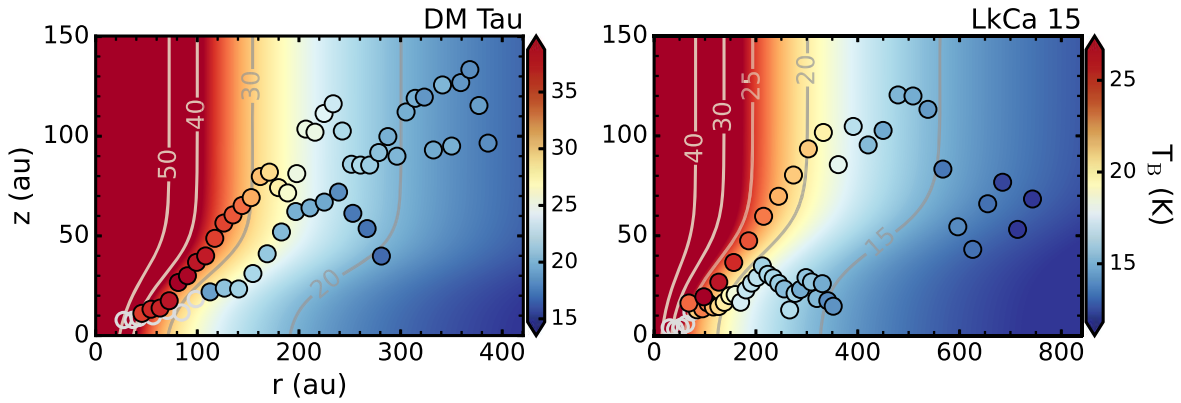
Figure 10. Comparison of the measured temperatures (points) with the fitted 2D temperature structures (background) for the DM Tau and LkCa 15 disks, as listed in Table 7. The same color scale is used for the data and fitted model in each panel. Points excluded from the fits are shown as hollow markers, while the scatter in the ^{13}CO surface at large radii in the DM Tau disk, which is also excluded from the fits, is not plotted for visual clarity. Contours show constant temperatures. The uncertainty of the temperature measurements, which is not shown here, can be found in Figure 9.

In the case of the LkCa 15 disk, since both $J = 3$–2 and $J = 2$–1 lines trace the same vertical layers, we chose to use the $J = 2$–1 line, which has a higher angular resolution. We only considered those regions with well-constrained temperature data in our fits, as shown in Figure 10. We also included all temperature data points, even those below $T_B < 20$ K in our fits. As gas temperatures close to or below the CO freeze-out temperature indicate that the line emission is likely partially optically thin, and thus a lower limit on the true gas temperature, we note that the true gas temperatures at large radii or closer to the disk midplane may be underestimated in our model.

Figure 10 shows the 2D fitted models in comparison with the data. For both disks, the residuals between the fitted model and measured temperatures are typically no more than 15%, with the exception of ^{13}CO in the DM Tau disk, where our model overpredicts gas temperatures by $\approx$25%–30%. As the emitting surfaces do not provide direct constraints in the disk midplanes, the empirically derived T_{mid} should be treated with caution.

The derived 2D temperature structure of the DM Tau disk is consistent with that of Flaherty et al. (2020), who used a similar two-layer model but a single power law for both T_{mid} and T_{atm} (i.e., $q = q_{mid} = q_{atm}$) and fixed values of α and β. Our model better captures the warmer temperatures along the inner (< 150 au) rising part of the CO emission surface. We also find a similar vertical temperature distribution in the LkCa 15 disk to that reported by Jin et al. (2019), who used an iterative, radiative-transfer model to derive the 3D disk temperature structure.[24] The primary difference is that the model of Jin et al. (2019) predicts a cooler disk midplane but, given our observational constraints as mentioned above, combined with the difficulty associated with deriving accurate midplane temperatures, this is not surprising.

5. Line emission Heights and Source Characteristics

Recent observations have demonstrated that line emission surfaces in protoplanetary disks exhibit a wide diversity in their vertical extent, degree of flaring, and even the potential presence of vertical substructures (Law et al. 2021a, 2022; Paneque-Carreño et al. 2023). While it is not yet clear what sets

this variety, one potentially promising way to gain further insight is by exploring links between line emission surface characteristics and source properties. In the five disk MAPS sample, Law et al. (2021a) first identified several tentative trends with various source parameters, such as more elevated surfaces in systems with lower stellar masses, cooler gas temperatures, and larger overall CO gas disks. In a larger sample of disks with mapped CO emission surfaces, Law et al. (2022) confirmed the presence of a tight correlation between CO line emitting heights and the CO gas disk size, while tentative trends with stellar host mass and gas temperature were consistent with expectations from simple scaling relations but showed substantial scatter. Here, we first revisit these trends in light of the newly derived emission surfaces in Section 5.1 and then we explore if ^{13}CO emission surfaces show any similar links with source properties in Section 5.2.

5.1. CO Emission Surfaces

To enable homogeneous, source-to-source comparisons, we first needed to compute the characteristic height of the newly derived emission surfaces. To do so, we adopted the definition introduced by Law et al. (2022), i.e., the mean of all z/r values interior to a cutoff radius of $r_{cutoff} = 0.8 \times r_{taper}$, where r_{taper} is the fitted parameter from the exponentially tapered power-law profiles from Table 3. This serves as a convenient definition, as averaging within 80% of the fitted r_{taper} ensures that we only include the rising portion of the emission surfaces, which we also visually confirmed for all surfaces. Since the CO $J = 2$–1 surface in the Sz 91 disk was fit with a single power-law profile, we manually fixed $r_{cutoff} = 300$ au to include only the rising portion of the surface. Since some disks are more flared than others, i.e., z/r changes rapidly with radius, we also computed the 16th to 84th percentile range within these same radii as a proxy of the overall flaring of each disk. Table 8 lists the characteristic z/r, flaring ranges, and r_{cutoff} values for all sources in our sample.

Figure 11 shows these representative z/r values for our disks and a large sample of literature sources as a function of stellar host mass, mean gas temperature, and CO gas disk size. All literature sources have directly mapped emission surfaces with source parameters derived in the same way as the disks in this work, i.e., dynamically derived masses from rotation maps, mean gas temperatures from directly mapped surfaces, and disk sizes computed as the radius enclosing 90% of the total flux

---

[24] The temperature structure shown in Jin et al. (2019, see their Figure 4), is in spherical coordinates and was first converted to cylindrical coordinates before comparing with our empirical temperature structure.

Table 8
Characteristic z/r of CO Isotopologue Emission Surfaces

Source	Line	$r_{\rm cutoff}$ (au)	z/r
This work:			
DM Tau	CO $J = 2-1$	229	0.41 (0.24, 0.48)
	^{13}CO $J = 2-1$	393[b]	0.22 (0.18, 0.30)
Sz 91	CO $J = 2-1$	300[a]	0.17 (0.15, 0.19)
LkCa 15	CO $J = 2-1$	456	0.26 (0.23, 0.30)
	^{13}CO $J = 2-1$	242	0.13 (0.10, 0.15)
	CO $J = 3-2$	450	0.23 (0.11, 0.27)
	^{13}CO $J = 3-2$	326	0.15 (0.13, 0.16)
HD 34282	CO $J = 2-1$	252	0.46 (0.32, 0.50)
	CO $J = 3-2$	404	0.38 (0.32, 0.53)
Literature:			
IM Lup	^{13}CO $J = 2-1$	339[b]	0.18 (0.12, 0.23)
GM Aur	^{13}CO $J = 2-1$	190	0.09 (0.05, 0.16)
AS 209	^{13}CO $J = 2-1$	163[b]	0.07 (0.02, 0.09)
HD 163296	^{13}CO $J = 2-1$	255	0.13 (0.08, 0.16)
MWC 480	^{13}CO $J = 2-1$	388[b]	0.05 (0.02, 0.09)
HD 97048	^{13}CO $J = 2-1$	367[b]	0.14 (0.08, 0.16)
Elias 2–27	^{13}CO $J = 3-2$	254[b]	0.33 (0.29, 0.37)

Notes. Literature sample composed of the disks around IM Lup, GM Aur, AS 209, HD 163296, and MWC 480 (Law et al. 2021a); HD 97048 (Law et al. 2022); and Elias 2–27 (Paneque-Carreño et al. 2021) with directly mapped ^{13}CO line emission surfaces. Only the west (uncontaminated) surface was used to calculate z/r in the Elias 2–27 disk. Characteristic z/r values are computed as the 50th percentile interior to $r_{\rm cutoff}$ and the 16th to 84th percentile range is shown in parentheses.
[a] Cutoff radius manually adjusted.
[b] Cutoff radius fixed to maximum radius where surface heights were derived, i.e., z/r is averaged over the entire surface radial range.

(Law et al. 2021a, 2021b, 2022; Paneque-Carreño et al. 2021; Rich et al. 2021; Teague et al. 2021; Veronesi et al. 2021).

Assuming that CO line emission surfaces scale with gas pressure scale heights, we expect that $z/r \sim M_*^{-1/8}$ and $z/r \sim T^{-1/6}$ (Law et al. 2022), as shown in orange in Figure 11. The size of the gas disk, $R_{\rm CO}$, and z/r were also shown to be tightly positively correlated (Law et al. 2022), as is evident in Figure 11. Here, we add two new sources (LkCa 15 and HD 34282) to these trends and refine the characteristic z/r value of the CO $J = 2-1$ surface of the DM Tau disk using new higher-angular-resolution observations.

The CO emission height of the LkCa 15 disk is consistent with all previous trends, while the HD 34282 disk appears to be an outlier with a CO emission surface with a characteristic z/r roughly a factor of 2 larger than expected for its stellar mass, disk gas temperature, and CO emission extent. Although we revise the characteristic z/r in the DM Tau disk down by $\approx 20\%$ from the value derived in Law et al. (2022), who used lower-angular-resolution data, it still shows the second-highest z/r of all known CO surfaces (with only the HD 34282 disk being more elevated).

Both stellar mass and mean temperature trends remain highly scattered and the weak trend suggested by scaling laws means that, even with additional sources, it is difficult to assess the reality of such trends. Observations of disks with more diverse properties, such as substantially warmer gas temperatures and around either lower-mass ($< 0.5\,M_\odot$) or higher-mass ($> 3\,M_\odot$) stars, are required to provide meaningful anchor points for these potential trends.

The correlation between $R_{\rm CO}$ and z/r remains strong and the addition of several sources with large CO disks allows us to

better quantify the $R_{\rm CO}$–z/r correlation. To do so, we used the Bayesian linear regression method of Kelly (2007) using the linmix Python implementation.[25] We find a best-fit relation of $z/r = (2.3 \pm 0.6 \times 10^{-4})R_{\rm CO} + (0.15 \pm 0.04)$ with a 0.04 scatter of the correlation (taken as the standard deviation σ of an assumed Gaussian distribution around the mean relation). We find a correlation coefficient of $\hat{\rho} = 0.77$ and associated confidence intervals of (0.27, 0.99), which represent the median and 99% confidence regions, respectively, of the 2.5×10^6 posterior samples for the regression. Overall, this is consistent with the fit reported by Law et al. (2022) but with a slightly less steep ($\approx 30\%$) slope.

Although not shown in Figure 11, the radially extended ($R_{\rm CO} \gtrsim 1400$ au) but modestly elevated ($z/r \sim 0.3$) edge-on CO disk around Gomez's Hamburger (Bujarrabal et al. 2009; Teague et al. 2020) may suggest a plateauing of z/r values in the largest of disks. Observations of more disks with extended CO gas disks (> 800 au) are required to discern if—and at what gas disk size—line emitting heights begin to plateau.

5.2. ^{13}CO Emission Surfaces

We also calculated the characteristic z/r for each of the ^{13}CO surfaces in our sample, as well as those in the literature from the MAPS disks (Law et al. 2021a) and the Elias 2–27 disk (Paneque-Carreño et al. 2021), which are listed in Table 8. For Elias 2–27, we only considered the uncontaminated western side of the disk to derive z/r and the radial size of the ^{13}CO emission. Similar to the CO $J = 2-1$ surface in the Sz 91 disk, the majority of ^{13}CO surfaces were either fit with a single power law or lacked a clear turnover in their surface (making previous fits of $r_{\rm taper}$ uncertain). Thus, for most disks we manually fixed the cutoff radii. In those cases where no plateauing of the surface was evident, we simply adopted the maximum radius for which a ^{13}CO line emitting height was derived as $r_{\rm cutoff}$ and averaged over the entire radial range of the surfaces.

Figure 11 shows a potential trend between the characteristic z/r of the ^{13}CO line emission surfaces with the stellar mass and mean ^{13}CO gas temperatures, respectively. In fact, these trends are considerably steeper than those predicted by simple scaling laws. To illustrate this, we overlay the approximate best-fit power laws to each trend in blue in Figure 11 and find that the z/r of the ^{13}CO surfaces traces $\sim M_*^{-3/4}$ and $\sim T_{\rm B}^{-1}$. We also find a tentative link between the size of the ^{13}CO gas disk and the z/r emitting height of ^{13}CO, which is approximately 4 times steeper in slope than that seen in CO. It is not immediately clear why the ^{13}CO trends are so much steeper those of CO, but it may be related to the fact that these disks are not, in fact, vertically isothermal.

Given the small sample size and difficulty in measuring the lower heights associated with ^{13}CO, it is possible that the apparent steepness of the ^{13}CO trends relative to CO is, at least in part, due to a biased disk sample. To test this idea, we removed those sources without corresponding ^{13}CO height measurements and reexamined the CO trends. We found that the mass and gas disk size trends are steeper than the full sample but are still not as steep as seen in ^{13}CO, while the gas temperature trend showed no additional steepening. While this may suggest the presence of a possible bias in the ^{13}CO disk sample, there still remains tentative evidence that the observed

---

[25] https://github.com/jmeyers314/linmix
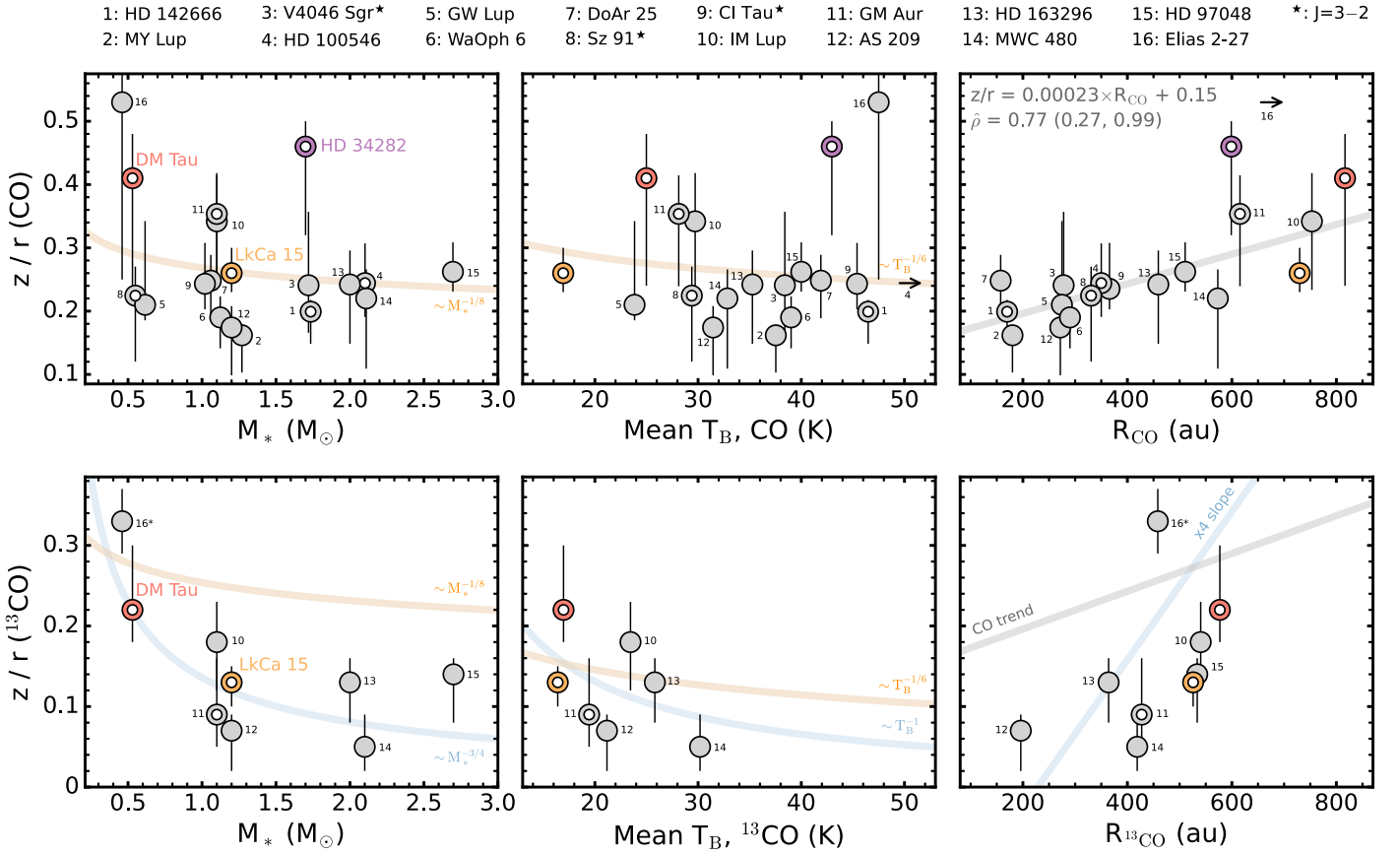
Figure 11. Characteristic z/r emission heights of CO (top row) and, when available, ^{13}CO (bottom row) vs. stellar mass, mean gas temperatures, and gas disk size (from left to right). All masses are derived dynamically, mean gas temperatures are computed over the same radial range in which z/r is determined, and gas disk sizes represent the radius containing 90% of the total flux. Annular markers indicate transition disks. Vertical lines show the 16th to 84th percentile range. All data are $J = 2-1$, except for those marked with a star (⋆), which are $J = 3-2$. All z/r measurements are from disks with directly mapped surfaces and compiled from HD 142666, MY Lup, V4046 Sgr, HD 100546, GW Lup, WaOph 6, DoAr 25, Sz 91, CI Tau (Law et al. 2022); IM Lup, GM Aur, AS 209, HD 163296, MWC 480 (Law et al. 2021a); HD 97048 (Rich et al. 2021; Law et al. 2022); and Elias 2–27 (Paneque-Carreño et al. 2021; Veronesi et al. 2021; Paneque-Carreño et al. 2022). The mean CO gas temperature in the HD 100546 disk is ≈130 K and, for the sake of visual clarity, is shown by a rightward arrow. The size of the Elias 2–27 CO gas disk is an approximate lower limit due to the system's complex emission morphology and severe cloud absorption (Huang et al. 2018b).

^{13}CO trends are tighter than those in CO. Firm conclusions are, however, limited by our small sample size, and additional high-spatial-resolution ^{13}CO line observations of disks are needed. Moreover, higher-angular-resolution observations of the HD 34282 disk would be useful in determining if the ^{13}CO surface in this source is also an outlier as in CO.

6. Conclusions

We present observations of CO, ^{13}CO, and C^{18}O emission in either or both $J = 2-1$ and $J = 3-2$ lines toward the DM Tau, Sz 91, LkCa 15, and HD 34282 disks at high spatial resolutions. We extracted line emission surfaces for all four transition disks in our sample and conclude the following:

1. CO emission surfaces generally trace elevated disk regions ($z/r \sim 0.2$–0.5), while the line emission heights of the less abundant ^{13}CO trace layers deeper into the disks ($z/r \lesssim 0.2$). The DM Tau and HD 34282 disks exhibit particularly elevated line emission surfaces.

2. In addition to vertical structure, we catalog all radial line emission structures present in all sources. With the exception of the DM Tau disk, most disks show a central dip or hole, a single line emission ring, and diffuse emission extending to large radii in multiple CO

isotopologues. The DM Tau disk also shows sharply centrally peaked line emission in all CO isotopologues.

3. We compared CO isotopologue line emission surfaces to the NIR scattering heights of micron-sized dust grains in the HD 34282 and LkCa 15 disks. In both disks, the NIR heights are comparable to that of the CO.

4. We compared emission surfaces derived from both the $J = 2-1$ and $J = 3-2$ lines in the same sources and found that in all cases, the surfaces lie at the same vertical heights. Since both lines are tracing the same disk layers, this suggests that the excitation differences in consecutive low-J rotational lines are insufficient to use them as tracers of multiple disk components.

5. We derived radial and vertical temperature distributions for all disks using all available CO isotopologue line emission surfaces. We estimated full 2D (r, z) empirical temperature models for the DM Tau and LkCa 15 disks.

6. By combining our sample with literature sources with previously mapped CO emission surfaces, we find that ^{13}CO emission surface heights show a tentative declining trend with stellar host mass and mean gas temperature that is considerably steeper than predicted by simple scaling laws. ^{13}CO emission surfaces also show a tentative positive correlation with gas disk size that is 4 times steeper than seen in CO. The CO emission surface

of the HD 34282 disk is a consistent outlier, showing a more elevated surface than expected for its given stellar mass, gas temperature, and gas disk size.

7. We derived dynamical masses for all sources in our sample using CO isotopologue rotational maps (see Appendix D). We find excellent agreement with mass estimates among different CO isotopologues and lines, with typical discrepancies of only $\lesssim 10\%$. This suggests that, provided it is sufficiently sensitive, an observation of only a single CO isotopologue line yields a robust dynamical mass for protoplanetary disk systems.

Appendix A
Atacama Large Millimeter/submillimeter Array Archival Observational Details

Table 9 lists all ALMA execution blocks used in this work and includes the ALMA project codes, PIs, covered CO isotopologues, UT observing dates, number of antennas, on-source integration times, baseline ranges, observatory-estimated spatial resolutions, maximum recoverable scales (M.R. S.), mean precipitable water vapor (PWV), and flux, phase, and bandpass calibrators. We also made use of ALMA data of LkCa 15 (2012.1.00870.S; PI: L. M. Pérez) from Jin et al. (2019) and HD 34282 (2013.1.00658.S; PI: G. van der Plas) from van der Plas et al. (2017). In each case, we obtained image cubes directly from the authors, rather than from the ALMA archive. A full description of these observations can be found in the corresponding references.

Table 9
Details of Archival ALMA Observations

Target	Project Code	PI	CO Isot., $J = 2$–1			UT Date	No. Ants.	Int. (min)	Baselines (m)	Res. (″)	M.R.S. (″)	PWV (mm)	Calibrators		
			CO	^{13}CO	C^{18}O								Flux	Phase	Bandpass
DM Tau	2013.1.00498.S	L. Pérez	Y	Y	Y	2015-8-12	44	14	15–1574	0.27	4.7	1.0	J0510+1800	J0510+1800	J0423-0120
	2016.1.00724.S	K. Flaherty	Y	Y	Y	2016-12-27	48	10	15–459	0.85	10.5	1.5	J0423-0120	J0510+1800	J0510+1800
			Y	Y	Y	2017-7-5	43	32	21–2647	0.26	3.9	0.6	J0423-0120	J0510+1800	J0510+1800
	2017.1.01460.S	J. Hashimoto	Y	Y	Y	2017-10-27	47	33	135–14851	0.03	1.1	0.5	J0510+1800	J0440+1437	J0510+1800
			Y	Y	Y	2017-10-27	47	33	135–14851	0.03	1.1	0.5	J0510+1800	J0440+1437	J0510+1800
Sz 91	2013.1.00663.S	H. Canovas	Y	Y	Y	2015-5-16	41	4	21–558	0.78	9.4	0.7	Titan	J1610-3958	J1517-2422
	2013.1.01020.S	T. Tsukagoshi	Y	Y	Y	2015-7-22	44	5	15–1574	0.29	3.3	2.7	J1517-243	J1610-3958	J1517-243
	2015.1.01301.S	J. Hashimoto	Y	Y	Y	2016-9-17	38	30	15–2483	0.20	4.3	0.7	J1517-2422	J1610-3958	J1517-2422
LkCa 15	2013.1.00226.S	K. Öberg	Y	Y	Y	2014-7-25	30	3	24–820	0.40	3.3	0.2	J0423-013	J0510+1800	J0510+1800
			Y	Y	Y	2014-7-29	31	12	24–820	0.39	3.1	0.9	J0510+180	J0510+1800	J0510+1800
			Y	Y	Y	2015-6-6	37	12	21–784	0.44	4.9	0.5	J0510+180	J0510+1800	J0510+1800
	2018.1.00945.S	C. Qi	N	Y	Y	2018-10-26	49	27	15–1398	0.38	11.2	0.6	J0510+1800	J0426+2327	J0510+1800
			N	Y	Y	2018-11-17	46	27	15–1398	0.38	11.2	1.6	J0510+1800	J0426+2327	J0510+1800
			N	Y	Y	2019-7-7	45	30	149–13894	0.03	1.3	1.4	J0510+1800	J0431+2037	J0510+1800
			N	Y	Y	2019-7-7	45	30	149–13894	0.03	1.3	1.4	J0510+1800	J0431+2037	J0510+1800
	2018.1.01255.S	M. Benisty	Y	N	N	2018-11-18	45	31	15–1398	0.35	7.6	0.5	J0510+1800	J0426+2327	J0510+1800
HD 34282	2015.1.00192.S	G. van der Plas	Y	Y	Y	2016-4-28	41	13	15–640	0.63	7.0	3.0	J0423-0120	J0542-0913	J0423-0120
			Y	Y	Y	2016-8-14	37	25	15–1462	0.31	6.3	0.6	J0423-0120	J0501-0159	J0522-3627
	2017.1.01578.S	J. de Boer	Y	Y	Y	2017-11-19	44	42	92–8548	0.05	1.2	0.6	J0423-0120	J0517-0520	J0423-0120
			Y	Y	Y	2017-11-19	44	42	92–8548	0.05	1.2	0.6	J0423-0120	J0517-0520	J0423-0120

Appendix B
CO Isotopologue Channel Maps

Channel maps of the CO $J = 2-1$ emission in the DM Tau disk are shown in Figure 12. A complete gallery of channel maps for each disk and all CO isotopologue lines is available in the electronic edition of the journal.
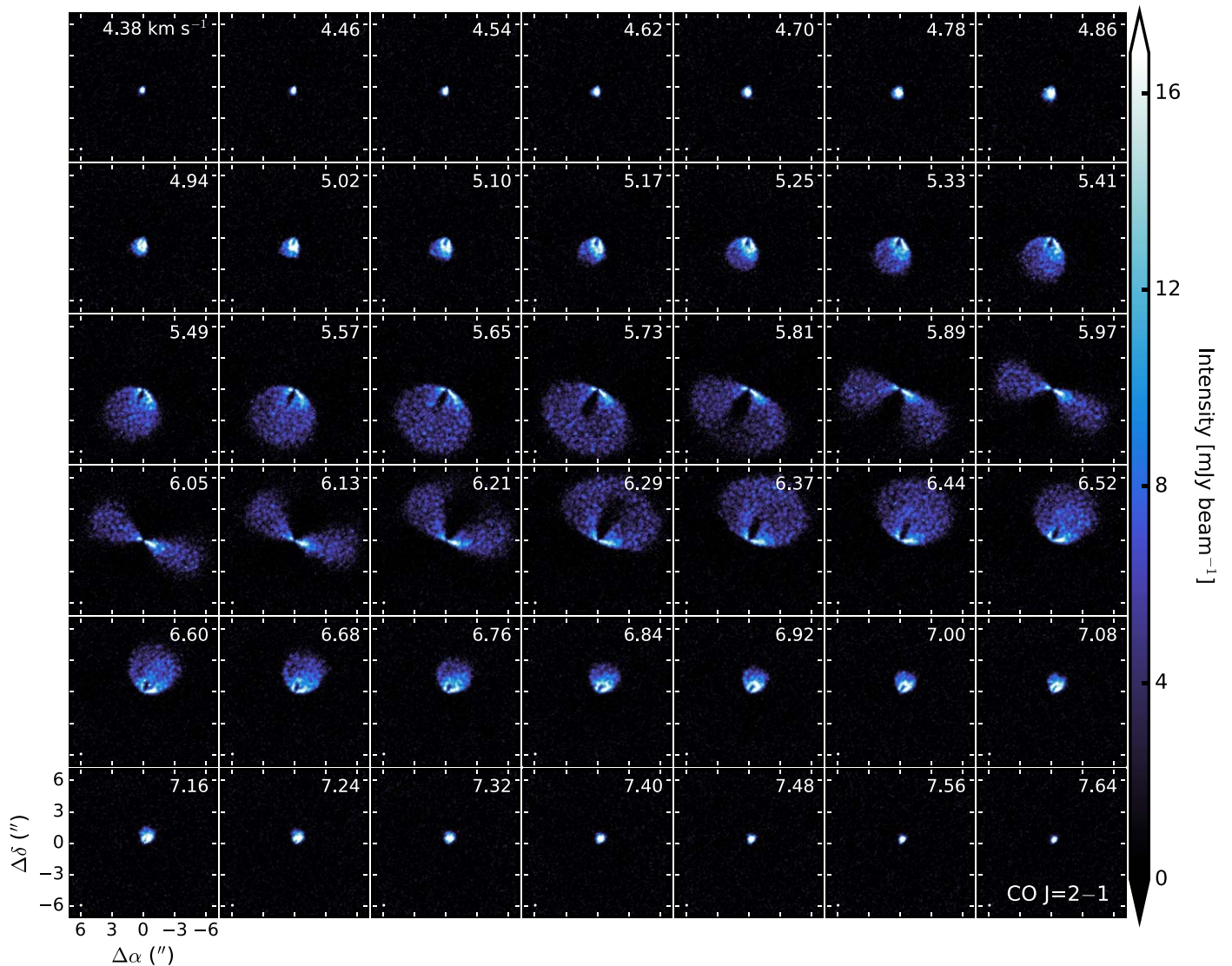
Figure 12. Channel maps of the CO $J = 2-1$ emission in the DM Tau disk. For the sake of visual clarity, only every second velocity channel is shown. The synthesized beam is shown in the lower left corner of each panel and the LSRK velocity in kilometers per second is printed in the upper right.

(The complete figure set (12 images) is available.)

Appendix C
Deriving Small Dust Scattering Heights in the LkCa 15 Disk

We measured the height of the second scattered light ring (66 au) in the LkCa 15 disk by fitting an ellipse to the peak flux using the SPHERE IRDIS *J*-band, Q_ϕ polarimetric image from Thalmann et al. (2016). This method was similar to the one used to measure the height of the scattered light rings around the HD 97048 disk (Rich et al. 2021). In summary, the peaks of the scattered light ring are found by taking radial slices every 1° between 0."22 and 1."7 from the location of the central star and finding the local maximum. The local maximum was not used if there was no minimum between the local maximum and the star to avoid measuring the location of the inner ring. We fit the local maximum points with an ellipse using the `EllipseModel` task from scikit-image and measured a minor axis offset of 0."0800 ± 0."0005. We estimated the uncertainties of the ellipse fit via bootstrapping and used 10% of the local maximum points 100 times. We assumed a disk inclination (50°2) and distance (157 pc) and calculated a height of the disk at 16.35 ± 0.12 au at a radius of 66.6 ± 0.2 au. We also measured the disk major axis PA (62°2 ± 0°2) and disk inclination (48°8 ± 0°1), which are consistent with previous measurements of the system (Oh et al. 2016; Currie et al. 2019; Blakely et al. 2022). Figure 13 shows the fitted ellipse plotted over the scattered light image of the LkCa 15 disk.
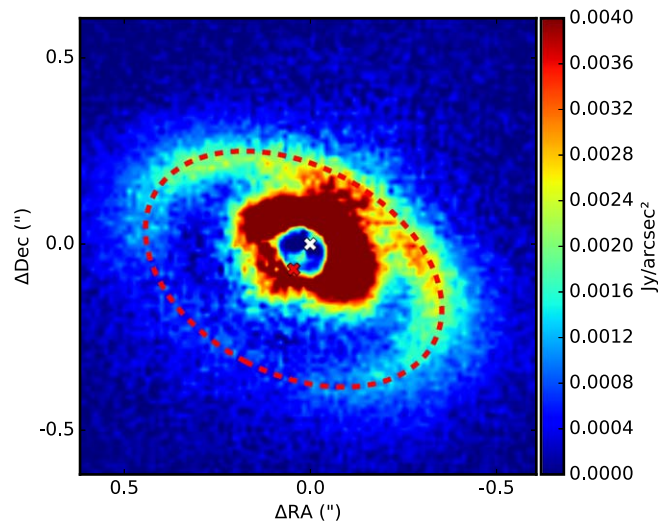
Figure 13. SPHERE IRDIS *J*-band imaging polarimetry (Q_ϕ) of the LkCa 15 disk from Thalmann et al. (2016) with the best-fit ellipse (dashed red line) to the 66 au ring. The location of the star (white cross) and the center of the ellipse (red cross) are marked on the image.

Appendix D
Dynamical Stellar Masses

We derived dynamical stellar masses for all sources in our sample using CO isotopologue rotation maps. As we have access to a complete suite of CO isotopologues, we computed the dynamical masses for each line individually and compared the relative consistency of the results. To do so, we closely followed the procedures outlined in Teague et al. (2021), which we briefly describe below.

We first generated maps of the line center (v_0), which include associated statistical uncertainty maps, using the "quadratic" method of bettermoments (Teague & Foreman-Mackey 2018), and then filtered these maps to only include regions where the peak intensities exceeded 5 times the rms. The resulting rotation maps were then fitted with eddy (Teague 2019b), which uses the emcee (Foreman-Mackey et al. 2013) python code for MCMC sampling. We considered three free parameters when modeling the Keplerian velocity fields: the disk PA, host star mass (M_*), and systemic velocity (v_{lsr}). The disk inclination (i) and emission surfaces, parameterized by z_0, ϕ, r_{taper}, and ψ (Equation (1)), were held fixed. Inclinations were adopted from literature values from Table 1, and surfaces were taken from the fits in Table 3. In the case of lines where surfaces could not be derived, we assumed the line emission originated from the disk midplane. For each disk, we fitted the continuum image with a single Gaussian profile using the imfit task in CASA to find the source offset from the phase center (δx_0, δy_0), which was then held fixed when using eddy with the exception of the HD 34282 disk. This source exhibits asymmetric continuum emission, which may skew the continuum fit, and we allowed (δx_0, δy_0) to remain as additional free parameters when fitting the $C^{18}O$ $J = 2-1$ rotation map. As $C^{18}O$ originates from close to the midplane, the assumption of a flat emission surface allows for an accurate determination of the disk center. The offsets derived using the $C^{18}O$ $J = 2-1$ line in the HD 34282 disk were adopted and then held fixed when

fitting CO and ^{13}CO $J = 2-1$ lines in the same disk. For the CO $J = 3-2$ line, we fixed the disk center to that inferred from the simple component ring fit to the continuum from van der Plas et al. (2017). For each disk, the innermost two beams were masked to avoid confusion from beam dilution. The outermost radii were set by a combination of S/N and the desire to avoid contamination from the rear side of the disk. Table 10 lists the selected values. The uncertainty maps produced by bettermoments were adopted as the uncertainties during the fitting.

We used 64 walkers to explore the posterior distributions of the free parameters, which take 500 steps to burn in and an additional 500 steps to sample the posterior distribution function. The posterior distributions were approximately Gaussian for all parameters, with minimal covariance between other parameters. Thus, we took model parameters as the 50th percentiles, and the 16th to 84th percentile ranges as the statistical uncertainties. Table 10 lists the fitted values and uncertainties for all disks.

For several sources and lines we restricted the regions of the rotation maps considered in the eddy fittings using manually determined wedges. This was necessary to exclude velocity signatures from the back side of the disk in DM Tau (CO $J = 2-1$) and LkCa 15 (CO $J = 2-1$, 3–2), as well as to avoid cloud contamination in the Sz 91 disk (CO $J = 2-1$). For all other sources and lines, we used the full azimuthal extents of the rotation maps. Figure 14 shows all rotation maps and the fitting regions used in eddy.

Figure 15 shows all derived dynamical masses for the sources in our sample. We also included the dynamical mass measurement from CO $J = 3-2$ in the Sz 91 disk, which was derived via eddy fitting in Law et al. (2022). In general, we find excellent agreement with mass estimates among different CO isotopologues and lines, with typical discrepancies of $\lesssim 10\%$. This is generally consistent with the variation observed in previous studies (e.g., Piétu et al. 2007; Premnath et al. 2020; Pegues et al. 2021). The largest differences ($\approx 40\%$) are seen in the Sz 91 disk, which is unsurprising considering that

Table 10
Best-fit v_{kep} Models

Source	Line	δx_0 (mas)	δy_0 (mas)	PA (°)	M_* ($M_\odot$)	v_{LSR} (km s^{-1})	$r_{fit,in}$ ($''$)	$r_{fit,out}$ ($''$)
DM Tau	CO $J = 2-1$[a]	[0.0]	[−1.4]	334.4 ± 0.14	0.52 ± 0.001	6.02 ± 0.001	[0.25]	[6.13]
	^{13}CO $J = 2-1$	[0.0]	[−1.4]	336.4 ± 0.08	0.55 ± 0.002	5.94 ± 0.001	[0.39]	[4.23]
	$C^{18}O$ $J = 2-1$	[0.0]	[−1.4]	336.6 ± 0.13	0.51 ± 0.002	6.02 ± 0.001	[0.40]	[3.16]
Sz 91	CO $J = 2-1$[b]	[0.0]	[−8.3]	193.4 ± 0.24	0.44 ± 0.006	3.38 ± 0.005	[0.46]	[2.42]
	^{13}CO $J = 2-1$	[0.0]	[−8.3]	196.8 ± 0.35	0.52 ± 0.005	3.33 ± 0.005	[0.48]	[2.12]
	$C^{18}O$ $J = 2-1$	[0.0]	[−8.3]	204.7 ± 0.49	0.64 ± 0.010	3.44 ± 0.007	[0.83]	[2.65]
LkCa 15	CO $J = 2-1$[a]	[0.0]	[−1.1]	64.7 ± 0.21	1.15 ± 0.007	6.25 ± 0.004	[0.73]	[4.73]
	^{13}CO $J = 2-1$	[0.0]	[−1.1]	61.4 ± 0.11	1.18 ± 0.004	6.20 ± 0.002	[0.28]	[3.88]
	$C^{18}O$ $J = 2-1$	[0.0]	[−1.1]	61.1 ± 0.10	1.15 ± 0.004	6.28 ± 0.002	[0.36]	[3.34]
	CO $J = 3-2$	[−2.5]	[−160.7]	60.5 ± 0.43	1.20 ± 0.010	6.31 ± 0.009	[0.72]	[2.87]
	^{13}CO $J = 3-2$	[−2.5]	[−160.7]	62.8 ± 0.15	1.24 ± 0.006	6.30 ± 0.003	[0.57]	[3.11]
	$C^{18}O$ $J = 3-2$	[−2.5]	[−160.7]	61.5 ± 0.78	1.26 ± 0.024	6.31 ± 0.016	[0.59]	[2.02]
HD 34282	CO $J = 2-1$	[−66.1]	[29.4]	115.6 ± 0.04	1.70 ± 0.003	−2.34 ± 0.001	[0.23]	[2.01]
	^{13}CO $J = 2-1$	[−66.1]	[29.4]	118.5 ± 0.07	1.67 ± 0.003	−2.37 ± 0.002	[0.25]	[1.48]
	$C^{18}O$ $J = 2-1$	−66.1	29.4	119.8 ± 0.07	1.72 ± 0.004	−2.34 ± 0.002	[0.25]	[1.36]
	CO $J = 3-2$	[−46.0][c]	[22.0][c]	114.6 ± 0.15	1.66 ± 0.008	−2.35 ± 0.003	[0.52]	[2.08]

Notes. Uncertainties represent the 16th to 84th percentiles of the posterior distribution. Values in brackets were held fixed during fitting.
[a] Due to conspicuous velocity signatures from the back side of the disk, fits were performed using manually drawn wedges.
[b] Due to cloud contamination, manual wedges were used in the fits.
[c] Disk center fixed to the single component ring fit to the continuum from van der Plas et al. (2017).
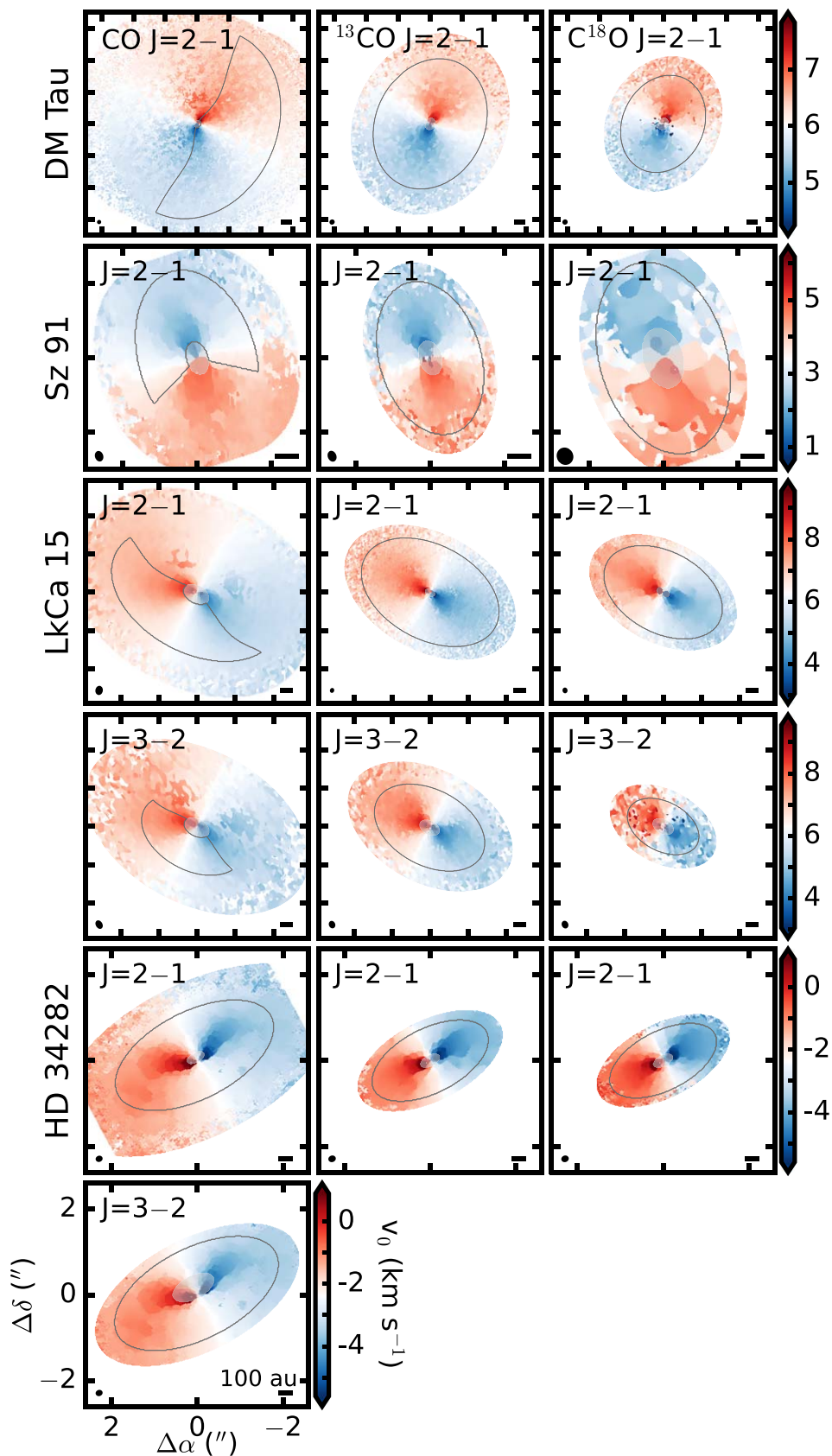
Figure 14. Gallery of rotation maps of CO, ^{13}CO, and C^{18}O emission in our disk sample. Panels for each disk have the same field of view, with each tick mark representing 2″. The innermost two beams, which are excluded from the fits, are shaded, while the outermost fitting radius is marked by a solid gray line. Wedges used in the fitting are shown for those sources where velocity signatures from both the front and back sides are clearly visible (CO $J = 2$–1 in DM Tau and CO $J = 2$–1, 3–2 in LkCa 15) or where foreground cloud absorption is present (CO $J = 2$–1 in Sz 91). The same velocity range is shown for each source and set of CO isotopologue lines. The synthesized beam and a scale bar indicating 100 au is shown in the lower left and lower right corner, respectively, of each panel.
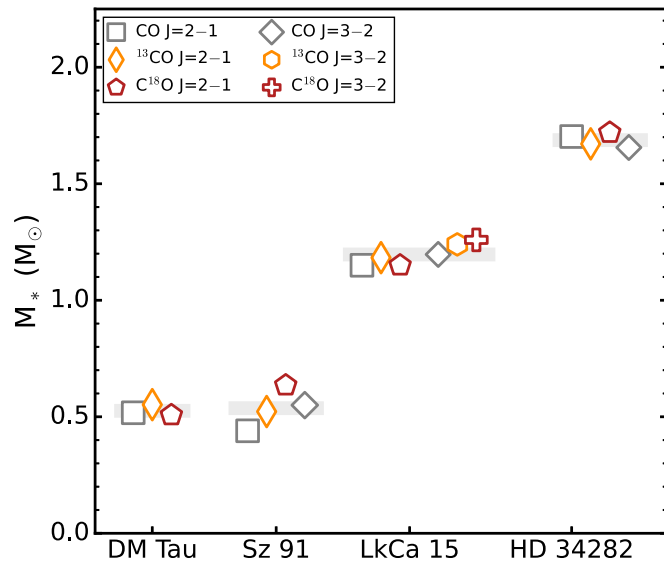
Figure 15. Dynamical stellar masses derived from rotation maps of CO isotopologue emission. The CO $J = 3$–2 mass measurement for the Sz 91 disk is taken from Law et al. (2022), while all others are computed in this work. The mean mass of all available measurements is shown as a shaded gray line and listed in Table 1.

both CO $J = 2$–1 and $J = 3$–2 lines are affected by cloud contamination and the $C^{18}O$ rotation map has the lowest angular resolution and S/N of any line considered in this sample. Overall, this implies that an observation of a single CO isotopologue line, provided it is sufficiently sensitive, yields a robust dynamical mass.

ORCID iDs

Charles J. Law ⬡ https://orcid.org/0000-0003-1413-1776
Richard Teague ⬡ https://orcid.org/0000-0003-1534-5186
Karin I. Öberg ⬡ https://orcid.org/0000-0001-8798-1347
Evan A. Rich ⬡ https://orcid.org/0000-0002-1779-8181
Sean M. Andrews ⬡ https://orcid.org/0000-0003-2253-2270
Jaehan Bae ⬡ https://orcid.org/0000-0001-7258-770X
Myriam Benisty ⬡ https://orcid.org/0000-0002-7695-7605
Stefano Facchini ⬡ https://orcid.org/0000-0003-4689-2684
Kevin Flaherty ⬡ https://orcid.org/0000-0003-2657-1314
Andrea Isella ⬡ https://orcid.org/0000-0001-8061-2207
Sheng Jin ⬡ https://orcid.org/0000-0002-9063-5987
Jun Hashimoto ⬡ https://orcid.org/0000-0002-3053-3575
Jane Huang ⬡ https://orcid.org/0000-0001-6947-6072
Ryan A. Loomis ⬡ https://orcid.org/0000-0002-8932-1219
Feng Long ⬡ https://orcid.org/0000-0002-7607-719X
Carlos E. Muñoz-Romero ⬡ https://orcid.org/0000-0001-7152-9794
Teresa Paneque-Carreño ⬡ https://orcid.org/0000-0002-4044-8016
Laura M. Pérez ⬡ https://orcid.org/0000-0002-1199-9564
Chunhua Qi ⬡ https://orcid.org/0000-0001-8642-1786
Kamber R. Schwarz ⬡ https://orcid.org/0000-0002-6429-9457
Jochen Stadler ⬡ https://orcid.org/0000-0002-0491-143X
Takashi Tsukagoshi ⬡ https://orcid.org/0000-0002-6034-2892
David J. Wilner ⬡ https://orcid.org/0000-0003-1526-7587
Gerrit van der Plas ⬡ https://orcid.org/0000-0001-5688-187X

References

Alarcón, F., Bosman, A. D., Bergin, E. A., et al. 2021, ApJS, 257, 8
Ansdell, M., Williams, J. P., Trapman, L., et al. 2018, ApJ, 859, 21
Astropy Collaboration, Robitaille, T. P., Tollerud, E. J., et al. 2013, A&A, 558, A33
Avenhaus, H., Quanz, S. P., Garufi, A., et al. 2018, ApJ, 863, 44
Bae, J., Teague, R., & Zhu, Z. 2021, ApJ, 912, 56
Bailer-Jones, C. A. L., Rybizki, J., Fouesneau, M., Demleitner, M., & Andrae, R. 2021, AJ, 161, 147
Blakely, D., Francis, L., Johnstone, D., et al. 2022, ApJ, 931, 3
Boehler, Y., Weaver, E., Isella, A., et al. 2017, ApJ, 840, 60
Bollati, F., Lodato, G., Price, D. J., & Pinte, C. 2021, MNRAS, 504, 5444
Bruderer, S., van Dishoeck, E. F., Doty, S. D., & Herczeg, G. J. 2012, A&A, 541, A91
Bujarrabal, V., Young, K., & Castro-Carrizo, A. 2009, A&A, 500, 1077
Calahan, J. K., Bergin, E. A., Zhang, K., et al. 2021, ApJS, 257, 17
Calcino, J., Hilder, T., Price, D. J., et al. 2022, ApJL, 929, L25
Canovas, H., Caceres, C., Schreiber, M. R., et al. 2016, MNRAS, 458, L29
Canovas, H., Schreiber, M. R., Cáceres, C., et al. 2015, ApJ, 805, 21
Casassus, S., & Pérez, S. 2019, ApJL, 883, L41
Cieza, L. A., González-Ruilova, C., Hales, A. S., et al. 2021, MNRAS, 501, 2934
Currie, T., Marois, C., Cieza, L., et al. 2019, ApJL, 877, L3
Czekala, I., Loomis, R. A., Teague, R., et al. 2021, ApJS, 257, 2
Dartois, E., Dutrey, A., & Guilloteau, S. 2003, A&A, 399, 773
de Boer, J., Ginski, C., Chauvin, G., et al. 2021, A&A, 649, A25
de Gregorio-Monsalvo, I., Ménard, F., Dent, W., et al. 2013, A&A, 557, A133
Disk Dynamics Collaboration, Armitage, P. J., Bae, J., et al. 2020, arXiv:2009.04345
Donati, J. F., Bouvier, J., Alencar, S. H., et al. 2019, MNRAS, 483, L1
Dong, R., Liu, S.-Y., & Fung, J. 2019, ApJ, 870, 72
Dullemond, C. P., Isella, A., Andrews, S. M., Skobleva, I., & Dzyurkevich, N. 2020, A&A, 633, A137
Dutrey, A., Guilloteau, S., Piétu, V., et al. 2017, A&A, 607, A130
Facchini, S., Benisty, M., Bae, J., et al. 2020, A&A, 639, A121
Fedele, D., van Dishoeck, E. F., Kama, M., Bruderer, S., & Hogerheijde, M. R. 2016, A&A, 591, A95
Flaherty, K., Hughes, A. M., Simon, J. B., et al. 2020, ApJ, 895, 109
Flores, C., Duchêne, G., Wolff, S., et al. 2021, AJ, 161, 239
Foreman-Mackey, D., Hogg, D. W., Lang, D., & Goodman, J. 2013, PASP, 125, 306
Gaia Collaboration, Brown, A. G. A., Vallenari, A., et al. 2021, A&A, 649, A1
Garufi, A., Avenhaus, H., Pérez, S., et al. 2020, A&A, 633, A82
Ginski, C., Stolker, T., Pinilla, P., et al. 2016, A&A, 595, A112
Guzmán-Díaz, J., Mendigutía, I., Montesinos, B., et al. 2021, A&A, 650, A182
Hashimoto, J., Muto, T., Dong, R., et al. 2021, ApJ, 911, 5
Huang, J., Andrews, S. M., Dullemond, C. P., et al. 2018a, ApJL, 869, L42
Huang, J., Andrews, S. M., Pérez, L. M., et al. 2018b, ApJL, 869, L43
Hunter, J. D. 2007, CSE, 9, 90
Ilee, J. D., Walsh, C., Booth, A. S., et al. 2021, ApJS, 257, 9
Ilgner, M., Henning, T., Markwick, A. J., & Millar, T. J. 2004, A&A, 415, 643
Izquierdo, A. F., Facchini, S., Rosotti, G. P., van Dishoeck, E. F., & Testi, L. 2022, ApJ, 928, 2
Izquierdo, A. F., Testi, L., Facchini, S., Rosotti, G. P., & van Dishoeck, E. F. 2021, A&A, 650, A179
Jin, S., Isella, A., Huang, P., et al. 2019, ApJ, 881, 108
Jorsater, S., & van Moorsel, G. A. 1995, AJ, 110, 2037
Kelly, B. C. 2007, ApJ, 665, 1489
Keppler, M., Teague, R., Bae, J., et al. 2019, A&A, 625, A118
Kudo, T., Hashimoto, J., Muto, T., et al. 2018, ApJL, 868, L5
Law, C. J., Crystian, S., Teague, R., et al. 2022, ApJ, 932, 114
Law, C. J., Loomis, R. A., Teague, R., et al. 2021b, ApJS, 257, 3
Law, C. J., Teague, R., Loomis, R. A., et al. 2021a, ApJS, 257, 4
Leemker, M., Booth, A. S., van Dishoeck, E. F., et al. 2022, A&A, 663, A23
Long, F., Andrews, S. M., Rosotti, G., et al. 2022, ApJ, 931, 6
Marr, M., & Dong, R. 2022, ApJ, 930, 80
Maucó, K., Carrasco-González, C., Schreiber, M. R., et al. 2021, ApJ, 923, 128
Maucó, K., Olofsson, J., Canovas, H., et al. 2020, MNRAS, 492, 1531
McMullin, J. P., Waters, B., Schiebel, D., Young, W., & Golap, K. 2007, in ASP Conf. Ser. 376, Astronomical Data Analysis Software and Systems XVI, ed. R. A. Shaw, F. Hill, & D. J. Bell (San Francisco, CA: ASP), 127
Monnier, J. D., Harries, T. J., Aarnio, A., et al. 2017, ApJ, 838, 20
Morbidelli, A., Szulágyi, J., Crida, A., et al. 2014, Icar, 232, 266
Öberg, K. I., Guzmán, V. V., Walsh, C., et al. 2021, ApJS, 257, 1

Oh, D., Hashimoto, J., Tamura, M., et al. 2016, PASJ, 68, L3
Paneque-Carreño, T., Miotello, A., van Dishoeck, E. F., et al. 2022, A&A, 666, A168
Paneque-Carreño, T., Miotello, A., van Dishoeck, E. F., et al. 2023, A&A, 669, A126
Paneque-Carreño, T., Pérez, L. M., Benisty, M., et al. 2021, ApJ, 914, 88
Pegues, J., Czekala, I., Andrews, S. M., et al. 2021, ApJ, 908, 42
Pegues, J., Öberg, K. I., Bergner, J. B., et al. 2020, ApJ, 890, 142
Pérez, S., Casassus, S., & Benítez-Llambay, P. 2018, MNRAS, 480, L12
Pérez, S., Casassus, S., Hales, A., et al. 2020, ApJL, 889, L24
Perez, S., Dunhill, A., Casassus, S., et al. 2015, ApJL, 811, L5
Piétu, V., Dutrey, A., & Guilloteau, S. 2007, A&A, 467, 163
Pinte, C., Ménard, F., Duchêne, G., et al. 2018, A&A, 609, A47
Pinte, C., van der Plas, G., Ménard, F., et al. 2019, NatAs, 3, 1109
Podio, L., Garufi, A., Codella, C., et al. 2020, A&A, 642, L7
Premnath, P. H., Wu, Y.-L., Bowler, B. P., & Sheehan, P. D. 2020, RNAAS, 4, 100
Price-Whelan, A. M., Sipőcz, B. M., Günther, H. M., et al. 2018, AJ, 156, 123
Quiroz, J., Wallack, N. L., Ren, B., et al. 2022, ApJL, 924, L4
Rab, C., Kamp, I., Dominik, C., et al. 2020, A&A, 642, A165
Rich, E. A., Teague, R., Monnier, J. D., et al. 2021, ApJ, 913, 138
Romero, G. A., Schreiber, M. R., Cieza, L. A., et al. 2012, ApJ, 749, 79
Rosenfeld, K. A., Andrews, S. M., Hughes, A. M., Wilner, D. J., & Qi, C. 2013, ApJ, 774, 16
Rosotti, G. P., Ilee, J. D., Facchini, S., et al. 2021, MNRAS, 501, 3427
Ruíz-Rodríguez, D., Kastner, J., Hily-Blant, P., & Forveille, T. 2021, A&A, 646, A59
Schwarz, K. R., Calahan, J. K., Zhang, K., et al. 2021, ApJS, 257, 20
Semenov, D., & Wiebe, D. 2011, ApJS, 196, 25
Stapper, L. M., Hogerheijde, M. R., van Dishoeck, E. F., & Paneque-Carreño, T. 2023, A&A, 669, A158
Teague, R. 2019a, JOSS, 4, 1632
Teague, R. 2019b, JOSS, 4, 1220
Teague, R. 2020, richteague/keplerian_mask: Initial Release, v1.0, Zenodo, doi:10.5281/zenodo.4321137
Teague, R., Bae, J., Aikawa, Y., et al. 2021, ApJS, 257, 18
Teague, R., Bae, J., & Bergin, E. A. 2019, Natur, 574, 378
Teague, R., & Foreman-Mackey, D. 2018, Bettermoments: A Robust Method to Measure Line Centroids, v1.0, Zenodo, doi:10.5281/zenodo.1419754
Teague, R., Jankovic, M. R., Haworth, T. J., Qi, C., & Ilee, J. D. 2020, MNRAS, 495, 451
Teague, R., Law, C. J., Huang, J., & Meng, F. 2021, JOSS, 6, 3827
Thalmann, C., Janson, M., Garufi, A., et al. 2016, ApJL, 828, L17
Thalmann, C., Mulders, G. D., Janson, M., et al. 2015, ApJL, 808, L41
Tripathi, A., Andrews, S. M., Birnstiel, T., & Wilner, D. J. 2017, ApJ, 845, 44
Tsukagoshi, T., Momose, M., Kitamura, Y., et al. 2019, ApJ, 871, 5
van der Plas, G., Ménard, F., Canovas, H., et al. 2017, A&A, 607, A55
van der Walt, S., Colbert, S. C., & Varoquaux, G. 2011, CSE, 13, 22
van der Walt, S., Schönberger, J. L., Nunez-Iglesias, J., et al. 2014, PeerJ, 2, e453
Veronesi, B., Paneque-Carreño, T., Lodato, G., et al. 2021, ApJL, 914, L27
Villenave, M., Stapelfeldt, K. R., Duchêne, G., et al. 2022, ApJ, 930, 11
Vioque, M., Oudmaijer, R. D., Baines, D., Mendigutía, I., & Pérez-Martínez, R. 2018, A&A, 620, A128
Virtanen, P., Gommers, R., Oliphant, T. E., et al. 2020, NatMe, 17, 261
Weaver, E., Isella, A., & Boehler, Y. 2018, ApJ, 853, 113
Wölfer, L., Facchini, S., Kurtovic, N. T., et al. 2021, A&A, 648, A19
Yu, H., Teague, R., Bae, J., & Öberg, K. 2021, ApJL, 920, L33
Zhang, K., Booth, A. S., Law, C. J., et al. 2021, ApJS, 257, 5